Geophysical Journal International

Geophys. J. Int. (2021) **226,** 91–113
Advance Access publication 2021 February 06
GJI Geodynamics and Tectonics

doi: 10.1093/gji/ggab053

Glacial isostatic adjustment of the Pacific Coast of North America: the influence of lateral Earth structure

Maryam Yousefi [1,*] Glenn A. Milne[1] and Konstantin Latychev[2]

[1] *Department of Earth and Environmental Sciences, University of Ottawa, Ottawa, ON, K1N 6N5, Canada. E-mail: myous023@uottawa.ca*
[2] *Department of Earth and Planetary Sciences, Harvard University, Cambridge, MA 02138, USA*

Accepted 2021 February 4. Received 2021 February 2; in original form 2020 September 29

SUMMARY

The Pacific Coast of Central North America is a geodynamically complex region which has been subject to various geophysical processes operating on different timescales. Glacial isostatic adjustment (GIA), the ongoing deformational response of the solid Earth to past deglaciation, is an important geodynamic process in this region. In this study, we apply earth models with 3-D structure to determine if the inclusion of lateral structure can explain the poor performance of 1-D models in this region. Three different approaches are used to construct 3-D models of the Earth structure. For the first approach, we adopt an optimal 1-D viscosity structure from previous work and add lateral variations based on four global seismic shear wave velocity anomalies and two global lithosphere thickness models. The results based on these models indicate that the addition of lateral structure significantly impacts modelled RSL changes, but the data-model fits are not improved. The global seismic models are limited in spatial resolution and so two other approaches were considered to produce higher resolution models of 3-D structure: inserting a regional seismic model into two of the global seismic models and, explicitly incorporating regional structure of the Cascadia subduction zone and vicinity, that is the subducting slab, the overlying mantle wedge and the plate boundary interface. The results associated with these higher resolution models do not reveal any clear improvement in satisfying the RSL observations, suggesting that our estimates of lateral structure are inaccurate and/or the data-model misfits are primarily due to limitations in the adopted ice-loading history. The different realizations of 3-D Earth structure gives useful insight to uncertainty associated with this aspect of the GIA model. Our results indicate that improving constraints on the deglacial history of the southwest sector of the Cordilleran ice sheet is an important step towards developing more accurate of GIA models for this region.

Key words: Structure of the Earth; Loading of the Earth; Sea level change; North America; Rheology: mantle.

1 INTRODUCTION

The isostatic response of the Earth to the most recent global-scale deglaciation (approximately 21 000–7000 yr before present) dominates secular changes in land height, the gravity field and relative sea level (RSL) in formerly glaciated regions and adjacent areas (e.g. Clark *et al.* 1978; Mitrovica & Peltier 1989; Lambeck *et al.* 1998). The Pacific coast of North America was proximal to the Laurentian ice sheet and partially covered by the Cordilleran ice sheet during the last glacial period (Fig. S1) and thus is significantly influenced by this process, commonly termed glacial isostatic adjustment (GIA). The effect of GIA is reflected in various data types, including palaeo reconstructions of RSL change (e.g. Engelhart *et al.* 2015) and measurements of land motion determined via the Global Positioning System (GPS; e.g. Montillet *et al.* 2018). Numerous studies have applied RSL reconstructions to constrain two primary components of GIA models in this region: solid Earth viscosity structure and the regional ice loading history (James *et al.* 2000, 2005, 2009a, b; Clague & James 2002; Muhs *et al.* 2012; Roy & Peltier 2015; Yousefi *et al.* 2018). All of these studies are based on the conventional spherically symmetric earth models which consider only radially variable viscosity structure.

Due to the proximity of this coastline to an active plate boundary, which includes the Cascadia Subduction zone, the observations mentioned above are also affected by the associated tectonic activity. A major component of this signal is a result of the convergence and

* Department of Earth & Planetary Sciences, McGill University, Montreal, QC, H3A 0E8, Canada. E-mail: maryam.yousefi@mcgill.ca

subduction of the remnants of the ancient Farallon oceanic plate, that is the Juan de Fuca, Gorda and Explorer plates, beneath the North American Plate (Severinghaus & Atwater 1990). In order to use RSL and land motion observations to constrain GIA model parameters, it is first necessary to estimate and remove the contribution from tectonic processes.

In a comprehensive 1-D GIA study for the west coast of North America, Yousefi *et al.* (2018) constrained GIA model parameters using a regional RSL data set with geographic extent from northern Vancouver Island to southern California. They adopted a broad range of model parameters, comprised of 704 Earth viscosity models and 29 different ice history models to constrain these primary GIA model parameters. One aspect that was addressed in their study is the effect of tectonic activity on local RSL change in this area and its potential impact on the GIA parameter inferences. Their results suggest significant spatial variability in mantle viscosity with a preference of lower values in the northern sector and increasing values towards the south. They also showed that no single 1-D model can fit the entire data set, emphasizing the potential importance of lateral structure to accurately model the GIA response.

There has been increasing interest in applying 3-D earth models that can accommodate lateral viscosity structure when modelling the GIA response at regional scales (e.g. Paulson *et al.* 2007; Austermann *et al.* 2013; Van der Wal *et al.* 2013; Li *et al.* 2018; Milne *et al.* 2018; Kuchar *et al.* 2019; Wu & Van der Wal 2003; 2015). A common approach taken in most of these studies is the use of seismic velocity models to infer the lateral mantle viscosity variations. Clark *et al.* (2019) presented 3-D GIA modelling results for central Cascadia, from northern Washington to central Oregon. In particular, they considered the sensitivity of Holocene RSL predictions to a scaling factor used in the conversion of seismic velocity anomalies, from the global S40RTS model (Ritsema *et al.* 2011), to viscosity anomalies. Their results suggest a relatively low-viscosity asthenosphere ($\sim 8 \times 10^{19}$ Pa s) and higher viscosity values at mid-upper mantle depths (slightly higher than 10^{21} Pa s). Their results also highlight the significant impact of lateral viscosity variations on predicted Holocene RSL change in central Cascadia.

In this study, we expand and complement the results of Clark *et al.* (2019) by considering a larger study area that extends north to northern Vancouver Island and south to southern California. As noted in Yousefi *et al.* (2018), the RSL data from southern British Columbia represent the greatest challenge for model fitting due to the highly non-monotonic changes that are typical of sites close to the ice margin. Uncertainty and error in the ice loading history are important aspects to consider at these sites as well as the influence of lateral Earth structure. A second aspect of our study that also extends the work of Clark *et al.* (2019) is that we consider four seismic models in estimating the lateral viscosity structure of the region as well as two global models of lithosphere thickness. Thus, we can assess if the RSL data indicate a preference for a particular seismic model.

We also consider two different approaches to define higher resolution lateral structure in the region given the relatively low resolution of the (global) seismic models. As the first approach, we use a state-of-the-art regional shear-wave seismic velocity model (Hawley & Allen 2019) and integrate it with two of the global seismic models. Alternatively, we use information on the extent of the Cascadia slab (Blair *et al.* 2011) to define a high-viscosity slab beneath the North American plate and a low-viscosity region between the subducting slab and the overlying continental lithosphere, the so-called 'mantle wedge'. The Cascadia forearc mantle wedge is stagnant and heavily serpentinized owing to the fluids produced from the shallow dehydration of the young and warm slab (Brocher at al. 2003; Wada *et al.* 2008). The relatively small scale of the subducting slab and mantle wedge are not captured in the global seismic models. We evaluate the accuracy of these different 3-D viscosity models by comparing output to observations of RSL change.

2 METHODS

2.1 The RSL observations

We use two published compilations of sea level data sets along the Pacific coast of North America to evaluate the accuracy of the models developed in this study: one from Vancouver Island to Central California (Engelhart *et al.* 2015), and one from Central California to Southern California (Reynolds & Simms 2015). The specific distribution of sites was chosen based on various criteria such as tectonic setting and distance from the former ice sheet (Engelhart *et al.* 2015; Yousefi *et al.* 2018). Each site comprises a relative sea level data set including both sea level index points (SLIPs) and limiting data (freshwater and marine indicators) as illustrated in the original publications that the data are extracted from (Engelhart *et al.* 2015; Reynolds & Simms 2015). We note that only the location of index points and the corresponding average of these are plotted in Fig. 1. A key prerequisite for a robust comparison between model predictions and observations is that the RSL data reflect only the influence of GIA. Considering the potential contribution from a tectonic signal in this region, we use a version of the data set that is corrected for the effect of tectonics using uplift rate estimates based on last interglacial shoreline elevations (Yousefi *et al.* 2018, see their section 2.1.1 and Table 1 for more details on the applied tectonic rates).

2.2 The model

We apply a forward modelling approach using a numerical finite-volume method for computing the response of a self-gravitating, Maxwell (viscoelastic) Earth to a specified surface loading history (Latychev *et al.* 2005a). The model solves the underlying equations (e.g. Wu & Peltier 1982) to compute solid Earth deformation on a spherical tetrahedral grid and output surface observables such as vertical displacement, changes in gravity and relative sea level change. The global tetrahedral grid is a multilayered spherical structure with triangulated spherical surfaces at user defined depths. Each tetrahedron has four vertices, known as grid nodes. Computational grid consists of a total number of ∼17 million nodes and ∼94 million elements. A number of physical properties, including density, elastic Lamé parameters, and viscosity are allocated to each of the computational grid nodes. Lateral resolution of the global computational grid is ∼12–15 km at the top surface and decreases with depth, with an average spacing of ∼60 km at the core–mantle boundary. Similarly, the radial resolution of the grid is greatest near the surface (∼12 km) and decreases towards the core–mantle boundary (∼50 km).

The sea level calculator solves the generalized sea level equation (Mitrovica & Milne 2003; Kendall *et al.* 2005) and so accounts for the evolution of coastlines. The influence of Earth rotation on GIA observables is also built into the software (Milne & Mitrovica 1998; Mitrovica *et al.* 2005). Solving the sea level equation requires two key model inputs: an ice loading history and a viscoelastic model of the Earth. The ice loading component is a spatio-temporal model of thickness and extent of the Late Pleistocene ice sheets. The

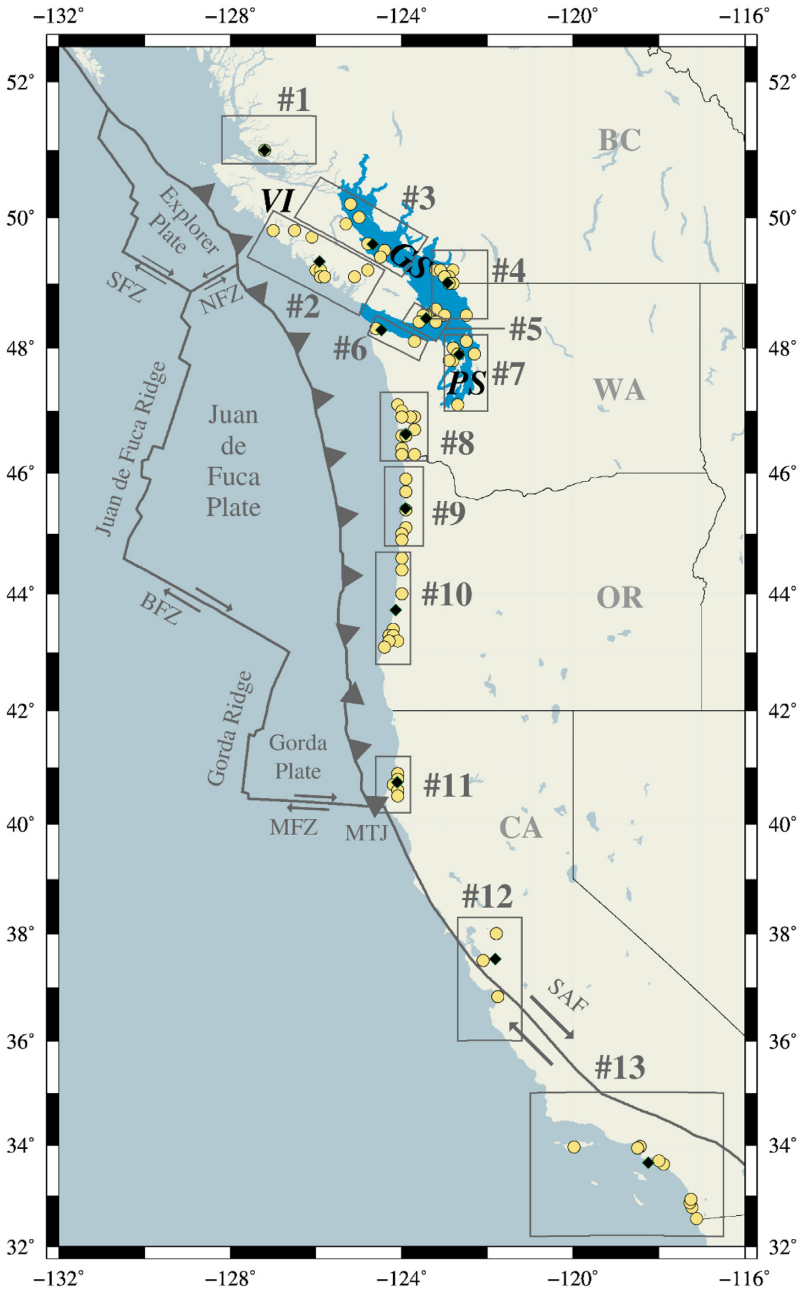

Figure 1. Map showing the spatial distribution of RSL data. The dark grey lines show plate boundaries, with the triangles indicating subduction of the Juan de Fuca, Explorer and Gorda plates beneath the North American Plate. The grey rectangles correspond to each of the 13 regions considered. The locations from where RSL data were acquired are indicated by yellow circles. The black diamonds in each region give the average location of the RSL data (index points only) for that region. MTJ represents the Mendocino Triple Junction; SFZ, BFZ, MFZ and NFZ represent the Sovanco, Blanco and Mendocino fracture zones and Nootka fault zone, respectively; SAF is the abbreviation for the San Andreas Fault; GS, PS and VI represent Georgia Strait, Puget Sound and Vancouver Island, respectively. U.S. states—Washington (WA), Oregon (OR) and California (CA)—and the Canadian province British Columbia (BC) are indicated along with their geographic boundaries (light grey lines). Shaded blue area around Vancouver Island marks the water boundary of the Salish Sea (Freelan, 2009; data retreived from https://erma.noaa.gov/northwest/erma.html).

ice loading model is established by projecting the ice thickness values on the surface nodal grid points of the global tetrahedral grid. We use a specific model '6885' selected from a large set of reconstructions of the North American Ice Sheet Complex (Tarasov *et al.* 2012) which is embedded in a background global model of ice evolution (ICE5G; Peltier 2004). The North American ice sheet reconstructions were simulated using a glacial systems model which includes a variety of physical processes related to ice sheet evolution in response to a defined climate forcing. Model output was calibrated against various types of regional observations such as RSL, ice extent, palaeo-lake levels and present-day crustal uplift rates. See Tarasov *et al.* (2012) for more detail on the glacial systems model and calibration procedure. We chose the 6885 ice model following the work of Yousefi *et al.* (2018) who showed that this particular ice loading history provides the best fit to the regional RSL data.

The 3-D viscoelastic earth models that we develop and apply here consist of a high viscosity lithosphere (to simulate an elastic medium on GIA timescale) with laterally variable thickness. We define the lateral variations in lithosphere thickness using two global models that are based on different approaches and observations as detailed in Section 2.2.1. We scaled the lithosphere thickness to a pre-defined value to enable comparison to output from 1-D models. In this study, this scaling results in a global average thickness of 46 km to be consistent with the optimal value inferred in the analysis of Yousefi *et al.* (2018). It is also compatible with the mean value inferred in a global analysis of RSL observations (Lambeck *et al.* 2014).

The lateral viscosity structure of the mantle is superimposed on a 1-D reference viscosity profile, which we describe below. In this study, three different approaches are used to define departures from our 1-D reference model: two give global estimates of 3-D viscosity structure with one of these approaches including a higher resolution regional model beneath our study region and the third approach includes lateral structure in our study region only (see Sections 2.2.2 and 2.2.3 for details on each approach). The density and elastic structure of the earth model are defined only in 1-D (with depth) and are given by the seismic model PREM (Dziewonski & Anderson 1981).

The viscous depth-structure of the reference 1-D model is the same as outlined in Yousefi *et al.* (2018) and is characterized by uniform viscosity within the upper mantle (below the lithosphere down to 670 km depth) and the lower mantle (from 670 km depth to the core–mantle boundary). Yousefi *et al.* (2018) divided their entire study area into three subregions: northern, from northern Vancouver Island to northern Washington; central, from southern Washington to southern Oregon; and southern, from northern California to southern California. Table S1 represents a summary of the optimal model parameters that were inferred using RSL data from each subregion, as well as those inferred from the entire data set. The parameters inferred using the entire data set are biased to northern sites given that the largest data-model residuals were found in this region. For this reason, we have chosen to not use this parameter set and use instead the optimal 1-D profile associated with the central region: (upper mantle viscosity (UMV) $= 2 \times 10^{20}$ Pa s, lower mantle viscosity (LMV) $= 10^{22}$ Pa s) as it is centrally located in our study area and is broadly consistent with a global analysis of RSL observations (Lambeck *et al.* 2014). Note, however, that we adopt the thinner lithosphere value (46 km) determined from considering the entire data set as the RSL data from central and southern regions are also fit relatively well using this value (Yousefi *et al.* 2018) and it is also more compatible with the global analysis of Lambeck *et al.* (2014). Some additional model runs were performed using a 1-D viscosity profile with a smaller increase in viscosity between the upper and lower mantle as found in other studies (e.g. Peltier 2004) and also supported by the data set considered in Lambeck *et al.* (2014). While the application of this model did produce different results, these differences are not large enough to impact the conclusions of our analysis.

2.2.1 Lithosphere thickness models

We apply two global models of lateral variations in lithosphere (elastic) thickness. One is the model presented by Zhong *et al.* (2003) which is a modified version of an earlier model (Watts 2001), hereafter referred to as the WA model, and the second is a model that we have constructed based on the global continental lithosphere model of Audet & Bürgmann (2011) which will be referred to as the AB model in the following. The continental lithosphere thickness in the WA model is estimated using a forward modelling technique based on the results of flexural loading studies. For oceanic regions, the elastic thickness depends on the thermal structure of the oceanic lithosphere (mainly controlled by its age) and is defined as the depth to the 750 °C isotherm (Zhong *et al.* 2003).

The AB model is a compilation of four components: a global model of oceanic lithospheric thickness, a global model of elastic thickness in continental areas (Audet & Bürgmann 2011) and two regional estimates of lithospheric thickness beneath Greenland (Steffen *et al.* 2018) and Antarctica (Chen *et al.* 2017). Over oceanic areas, we follow the formulations presented in Caldwell & Turcotte (1979) and assume that thermal structure and thickness of the lithosphere are functions of the square root of ocean-floor age. We apply a global seafloor age data set that is based on marine magnetic anomaly isochrones (Müller *et al.* 2008) and define the base of the oceanic lithosphere to correspond to the depth of the 700 °C isotherm as proposed by Caldwell & Turcotte (1979). The continental lithosphere elastic thickness in the AB model was estimated using an inverse modelling approach by computing the spectral coherence between topography and gravity anomalies and comparing it to model predictions (Audet & Bürgmann 2011). The model of Audet & Bürgmann (2011) covers all major continents except for Greenland and Antarctica. For this reason, we have included the regional models that use a similar inverse modelling technique to infer the elastic thickness beneath Greenland (Steffen *et al.* 2018) and Antarctica (Chen *et al.* 2017). Fig. 2 shows the lateral variations in lithospheric thickness at both global and regional scales and illustrates that there is generally good agreement between the two models. However, there are some differences, with the AB model showing markedly lower values in most regions except for Africa, North America and northwestern Eurasia. At the regional scale, the WA model represents considerably greater thickness values for the oceanic lithosphere reflecting the higher isotherm used to define the base of this layer. The differences observed between the two models can be primarily explained by the different methodologies applied and the improved data sets used in the more recent analyses. However, as mentioned in the previous section, the two models are scaled to give a global mean of 46 km to match our 1-D reference viscosity model.

2.2.2 Global viscosity structure

We apply four different global seismic tomography models to estimate lateral viscosity variations: S40RTS (Ritsema *et al.* 2011), Savani (Auer *et al.* 2014), SEMUCB-WM1 (French & Romanowicz 2014) and SL2013 (Schaeffer & Lebedev 2013). Each of these models provides variations (relative to a global mean reference model) in shear wave velocity throughout the whole mantle, except for SL2013 which does not extend below 1000 km depth. The variations in seismic wave velocities can be attributed to the variations in thermal and/or compositional structure. Assuming that the temperature is the only driving factor, we follow Latychev *et al.* (2005a) to determine the mantle viscosity structure using the following set of eqs (1)–(3):

$$\delta \ln \rho\,(r,\theta,\varphi) = \frac{\partial \ln \rho}{\partial \ln v_s}\,(r)\;\delta \ln v_s\,(r,\theta,\varphi) \tag{1}$$

$$\delta T\;(r,\theta,\varphi) = -\frac{1}{\alpha\,(r)}\,\delta \ln \rho\,(r,\theta,\varphi) \tag{2}$$

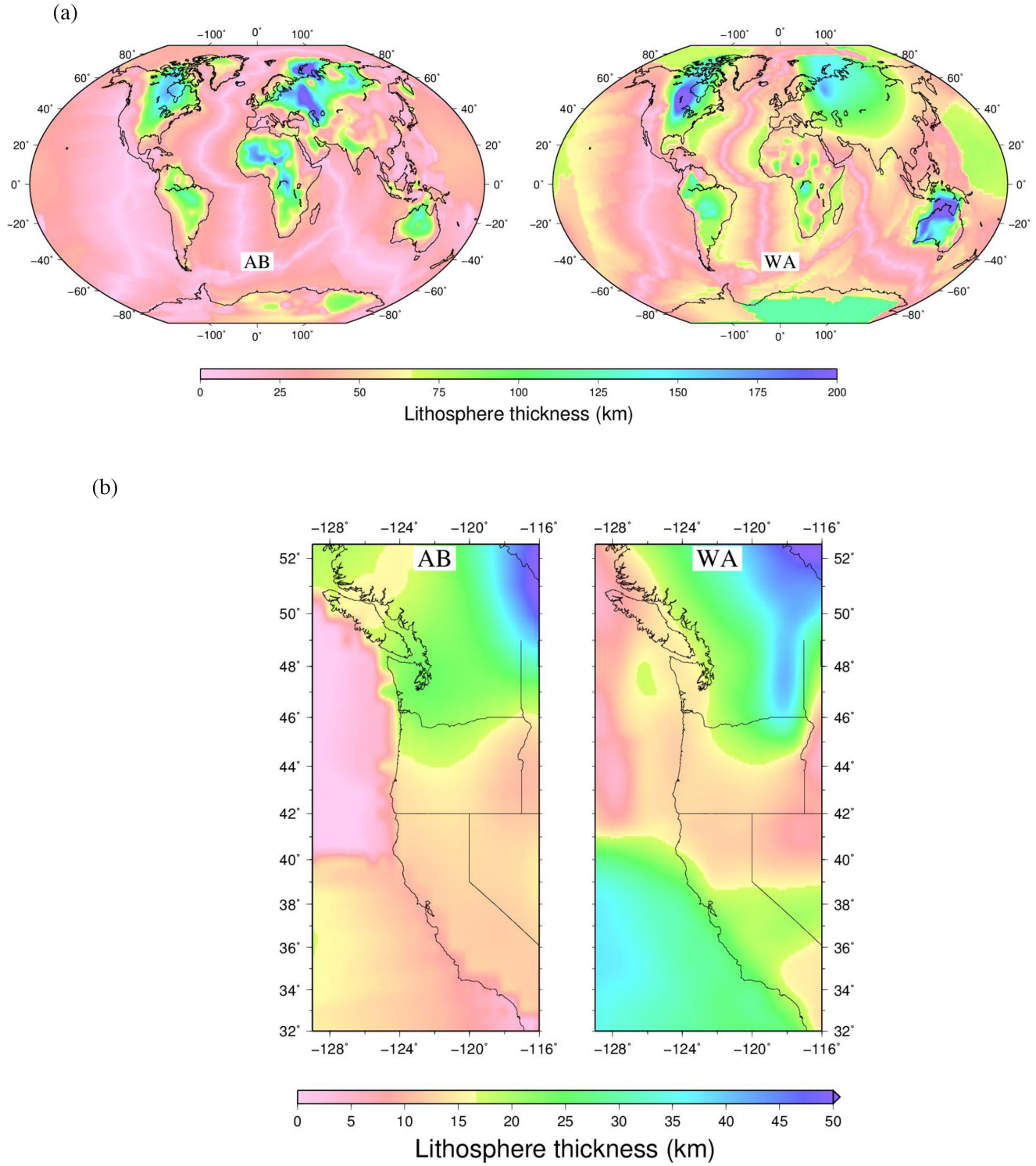

Figure 2. (a) Global and (b) regional elastic thickness variations of the lithosphere based on the global continental model of Audet & Bürgmann (2011), referred to as the AB model (left-hand panel) and that presented by Zhong *et al.* (2003) referred to as the WA model (right-hand panel). See text for further information.

$$\eta\ (r, \theta, \varphi) = \eta_0\ (r)\ e^{-\epsilon\, \delta T(r,\theta,\varphi)}, \tag{3}$$

where r, θ and φ are the radius, colatitude and east longitude, respectively. The term $\delta \ln v_s(r, \theta, \varphi)$ represents seismic shear wave velocity perturbations and $\frac{\partial \ln \rho}{\partial \ln v_s}(r)$ is a depth-dependant logarithmic scaling factor used to convert the velocity variations to density variations ($\delta \ln \rho$) (eq. 1). We adopt the radial profile of Forte & Woodward (1997) for the velocity-to-density scaling coefficient with an estimated range of ∼0.1–0.35. The variations in temperature (δT) are then calculated by scaling the density field using the

radially variable coefficient of thermal expansion, $\alpha(r)$ (eq. 2). The depth-dependent thermal expansion coefficient that we use here is based on the high-temperature, high-pressure laboratory experiments of Chopelas & Boehler (1992). Finally, the 3-D viscosity structure (η) is estimated using an exponential function of the scaled temperature anomalies (eq. 3). The scaling factor (ϵ) appearing in the exponent of eq. (3), determines the degree of dependence of the viscosity structure on temperature. We set this parameter to 0.04 $^{\circ}C^{-1}$, which results in the viscosity anomaly pattern illustrated in Fig. 3.

Fig. 3 shows the viscosity variations with respect to our reference viscosity profile defined above ($\eta_0(r)$, 2×10^{20} Pa s for the upper mantle, and 10^{22} Pa s for the lower mantle) associated with each seismic model at three different depths: 200, 600 and 1000 km. (Note that SL2013 is primarily an upper mantle model and so has, by construction, limited resolving power at 1000 km.) For each model, there is considerable spatial variability in the inferred viscosity variations at each indicated depth. The positive and negative anomaly values mainly reflect the long-wavelength heterogeneity of sublithospheric mantle features. For example, the relatively smooth gradient in the upper mantle viscosity, which shows lower viscosity values to the west, potentially arises from a hotter and shallower asthenosphere in comparison to the colder and more stable eastern section. The global velocity models generally lack sufficient resolution to image the shorter wavelength heterogeneity thought to exist in this region. Nevertheless, the higher viscosity anomalies evident in Fig. 3 can be attributed to the subducting Juan de Fuca-Gorda slab (200 km depth) and remnant fragments from the Farallon slab (600 km depth, e.g. Xue & Allen 2010; Obrebski *et al.* 2011). Furthermore, the localized high viscosity anomaly associated with the SEMUCB model in southern California at 200 km depth might be due to the presence of lithospheric material at the base of the asthenosphere resulting from the post-Laramide detachment of the lithospheric root (Zandt *et al.* 2004). We note that each of the seismic models use different data sets and modelling approaches which cause the differences evident in the inferred viscosity variations (Fig. 3). For further details about the data and methodology applied for producing each seismic model, please refer to the original publications cited above.

2.2.3 Regional viscosity structure

Given the relatively low resolution of the global seismic models introduced above, we used two alternative approaches to assign regional 3-D viscosity structure at higher spatial resolution. For the first approach, we use the regional shear wave seismic velocity model of Hawley & Allen (2019) and insert it into two of the global seismic models: S40RTS and SEMUCB-WM1. The lateral resolution of the regional seismic model is 0.25° (∼27 km) and covers the entire area enclosed within (31°N, 131°W) and (51°N, 101°W). This regional *S*-wave velocity model has a uniform radial resolution of 25 km from the Earth surface to 1000 km depth. The conversion from seismic velocity anomaly to viscosity variations for the regional model is based on the same procedure and parameter values detailed in Section 2.2.2 for the global models. The lateral viscosity variations generated by inserting the regional model into the S40RTS and SEMUCB global models are shown in Figs 4 and S2, respectively. Both of these composite models have a similar viscosity perturbation pattern but with some differences in amplitude which arise from the integration process that normalizes the regional average to match the global average and also the interpolation procedure that ensures a smooth transition in viscosity where the two models are joined.

From Fig. 4 it is evident that the regional model better resolves shorter-scale features that are not captured by the global models. An example of such a feature is the subducting slab causing the positive anomaly values as indicated in Fig. 4(a) which is also observed in a vertical cross section of the viscosity model at 47°N (Fig. 4b). Another feature is a relatively strong negative anomaly representing a buoyant low-viscosity layer beneath the downgoing slab which is mapped as a north–south red layer along the western side of the slab in Fig. 4. Although the integrated model reveals some of the shorter wavelength viscosity perturbations associated with the subduction-system, the amplitudes of the anomalies are considerably smaller than those expected in such a system (see following paragraphs in this section). For example, the subducting slab is characterized by positive anomaly values that are only two orders of magnitude greater than the background viscosity of the upper mantle.

As a second approach to build the regional 3-D viscosity structure, we explicitly consider the slab geometry and possible existence of a low viscosity mantle wedge above the slab. Specifically, we incorporate a high-viscosity (10^{26} Pa s) slab, a low-viscosity (10^{18} Pa s) mantle wedge and a plate boundary interface between the oceanic and the continental plates using a lithosphere viscosity of 1.7×10^{20} Pa s (Fig. 5). Thus, the model simulates plate boundaries as weak zones within the lithosphere. The locations of plate boundaries are defined using a digital map of global plate boundaries (Bird 2003) and our adopted viscosity value is compatible with that suggested in some studies (e.g. Lamb 2015). The width of the plate boundary is not constant and is defined using an adaptive tolerance based on the local lithosphere thickness with thicker lithosphere leading to a greater boundary width (although we define 96 km as the maximum width). The edges of plate boundaries are vertical except in the vicinity of a subducting slab where the boundary edge will run parallel to the surface of the slab within the overlying plate.

There are various factors that control the rheology of this regional structure, including temperature, water content and composition. Observations of surface heat flow indicate no evidence of anomalously high values within the forearc mantle wedge suggesting that this part of the mantle is stagnant and cold (Currie *et al.* 2004; Wada *et al.* 2008). However, the influx of water-rich fluids from the subducting oceanic plate into the overlying mantle wedge generates hydrous minerals, in particular serpentine, that could reduce the viscosity of the wedge corner (Hyndman & Peacock 2003). Although there is no direct evidence for the existence of low viscosity material within the mantle wedge, geodetic and geological constraints such as crustal strain rates and RSL observations suggest a viscosity value in range of 10^{18}–10^{19} Pa s (James *et al.* 2000; Clark *et al.* 2019; Wang *et al.* 1994; Yousefi *et al.* 2018). Our considered value for the mantle wedge viscosity (10^{18} Pa s) is in agreement with these previous studies. James *et al.* (2009a, b) suggest that for a 10–40-km-thick mantle wedge, effective viscosities in the range of 10^{15}–10^{17} Pa s would be required to effectively contribute to the observed sea level response. Therefore, we also examine the influence of a mantle wedge region with viscosity of 10^{15} Pa s.

Although we adopt a constant value of 10^{26} Pa s for the slab viscosity, in reality, this value is not constant with variations in the range of 10^{3}–10^{6} Pa s (Billen 2008). For this reason, we also perform an additional sensitivity test by reducing the slab viscosity to 10^{23} Pa s. The slab geometry is generated based on a gridded slab surface data set (Blair *et al.* 2011). This reconstruction of the

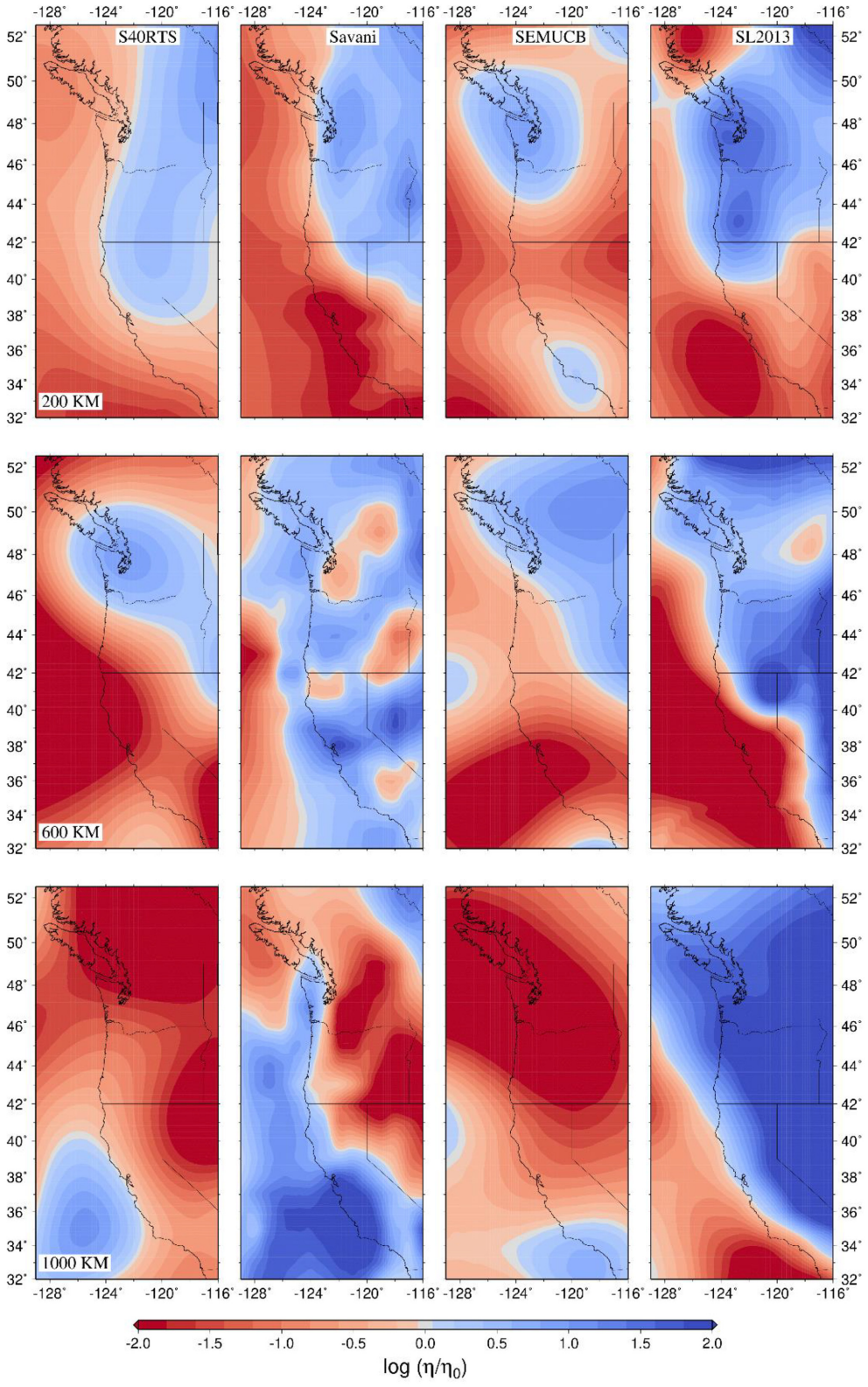

Figure 3. Lateral viscosity variations at depths of 200 km (top row), 600 km (middle row) and 1000 km (bottom row), associated with four global seismic models (from left-hand column to the right-hand column): S40RTS, Savani, SEMUCB-WM1 and SL2013. Note that these variations are relative to a chosen 1-D (radial) viscosity model [η_0(r)].

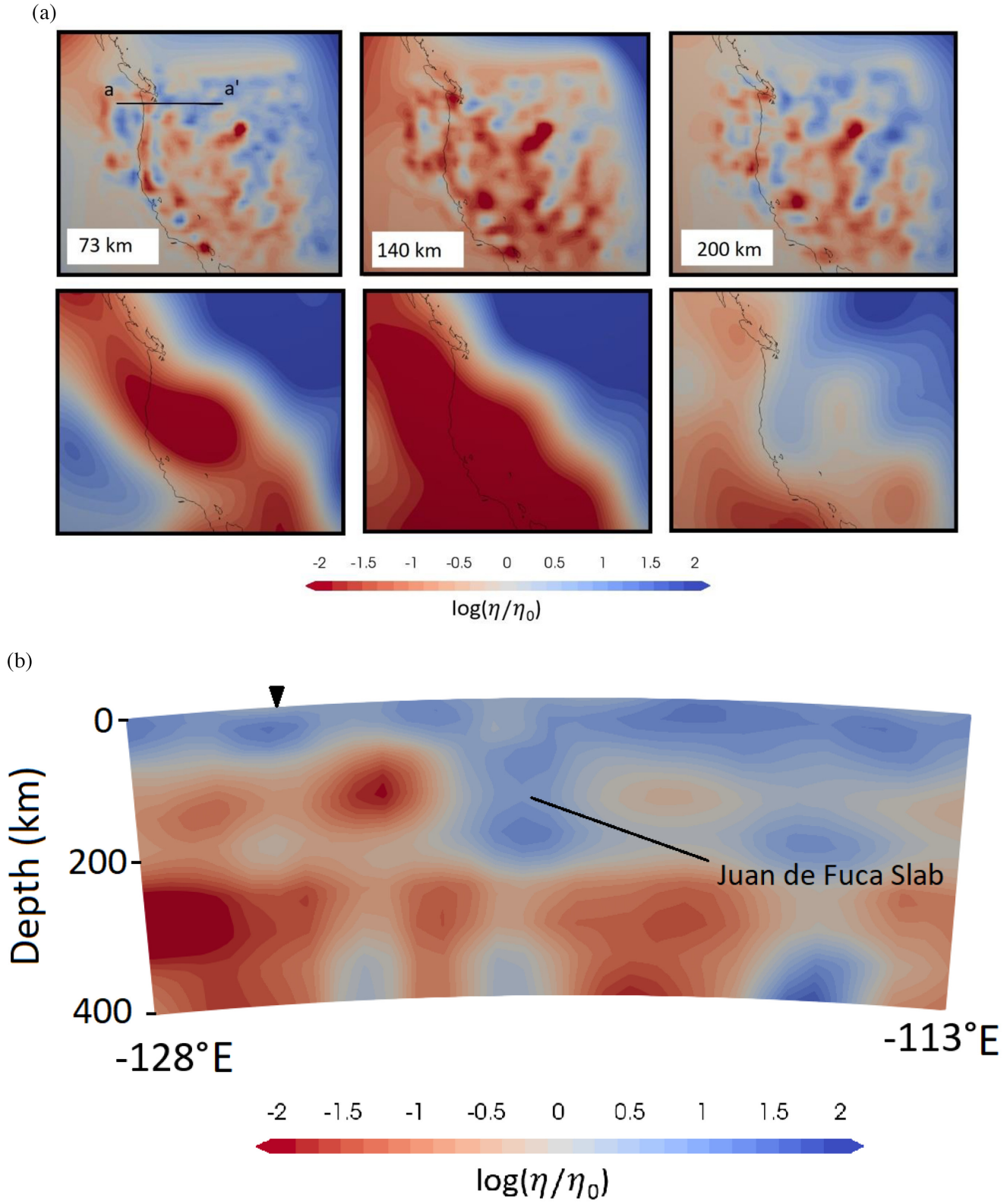

Figure 4. (a) Lateral viscosity anomalies at depths of 73, 140 and 200 km associated with (top row) the regional model of Hawley & Allen (2019) integrated with the global S40RTS model, (bottom row) the global S40RTS model. (b) A vertical cross section of the viscosity structure along the surface profile a–a' at 47° shown in (a). The inverse black triangle marks the approximate location of the trench.

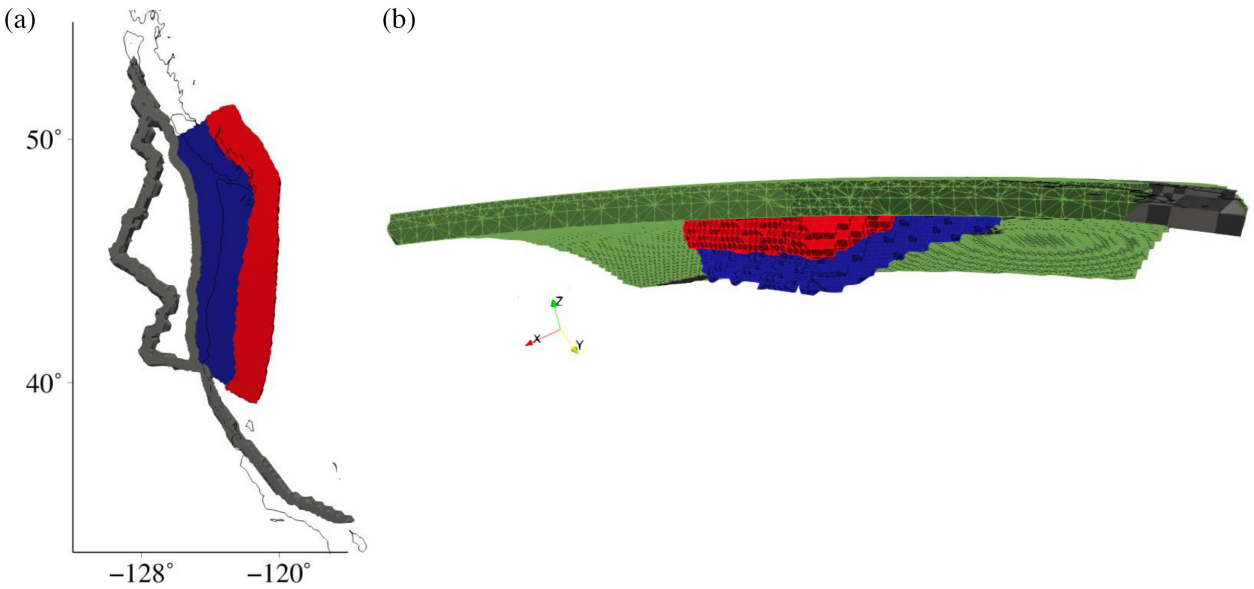

Figure 5. (a) Modelled regional structure of the Cascadia subduction zone in plan view: the subducting slab is shown in blue, the low-viscosity mantle wedge zone in red and the plate boundary in dark grey. (b) Alternative view of the structure shown in (a) looking south and including the objects presented in (a) as well as the lithosphere (green) which has a constant thickness of ∼46 km in this particular case. The plate boundary is confined within the lithosphere and is vertical everywhere except for the slab region where it runs parallel to the surface of the slab within the overlying plate. Note that the plate boundary is not distinguishable in (b) as it is within the lithosphere. These plots have been generated using Paraview software (Ahrens et al., 2005)

slab surface was primarily determined using three types of data: regional earthquake hypocentre profiles, teleseismic traveltime data and seismic reflection and refraction transects. We define the base of the slab by assuming that it is characterized by a uniform thickness of ∼55 km. The low-viscosity mantle wedge is then added as an elongated 3-D triangular volume between the downgoing oceanic slab and the overlying continental lithosphere (Fig. 5).

3 RESULTS AND DISCUSSION

In this section, we present results for the different realizations of the 3-D Earth structure described above. A complete list of these models along with their characteristics is shown in Table S2. Fig. 6 shows the net GIA signal as well as its associated loading components (i.e. the ice and ocean loads) to the spatial variation in RSL at 10 ka computed using the reference 1-D model. The ice loading dominates the GIA signal causing a net RSL rise in parts of southern British Columbia and net RSL fall in the rest of the study area since 10 ka. The ocean loading component (Fig. 6c), produces a tilting pattern with a net RSL rise offshore and RSL fall at onshore locations which reflects the effect of continental levering (Clark *et al.* 1978; Mitrovica *et al.* 2001). In order to quantify the influence of lateral viscosity structure on the predicted RSL change, we use the results in Fig. 6(a) as a reference case that output from models with 3-D viscous structure are compared to in the following.

3.1 3-D global earth models

Fig. 7 shows the effect of sublithosphere mantle viscosity structure on modelled RSL at 10 ka associated with four different global seismic models as well as the influence of variations in lithosphere thickness. The effect of sublithosphere variability in mantle viscosity results in a long wavelength pattern of RSL change that generally lies within ±10 m of the 1-D model results along the coastline. Although there are some similarities between the contribution from each global viscosity model, such as the positive RSL departure from the 1-D reference model in northern California and southern Oregon, there are also differences in both sign and magnitude. For example, the Savani model results in negative RSL anomalies along the coasts of British Columbia, Washington, and northern Oregon, whereas the other models generally produce positive values in these areas. Another example is the negative RSL values in central and southern California associated with the SL2013 model, while the other models give a positive departure from the 1-D model output. In comparison to the effect of the sublithosphere mantle structure, adding laterally variable lithosphere thickness causes shorter-scale RSL spatial anomalies with greater amplitude (lower-panel plots in Fig. 7). The high positive RSL values relative to the 1-D model exceeding 30 m in northcentral Vancouver Island (northern Salish Sea) is one good example of this shorter wavelength but higher amplitude change. The RSL signals associated with the two different lithosphere models generally follow similar patterns with some notable amplitude differences, especially in the Vancouver Island area. This discrepancy reflects the effect of the thicker/thinner lithosphere in damping/amplifying the Earth response to the applied ice loading.

The combined influence of lateral mantle viscosity variations and laterally variable lithosphere structure associated with the AB model on RSL relative to the 1-D case is plotted in Fig. 8. Fig. S3 shows the same results as Fig. 8 but for the WA lithosphere model. Building on our discussion of the results in Fig. 7, comparable interpretations apply to Figs 8 and S3: the longer-wavelength variations can be attributed to the sublithosphere viscosity structure and the smaller-scale, often higher-amplitude RSL signals, particularly around Vancouver Island, originate from lateral variations in lithosphere thickness. The influence of lateral structure is less than 10 m along the coast from southern Washington to southern California for all models except for the S40RTS model which results in slightly higher RSL values (10–20 m) in Washington and Oregon states. In the northern region, however, greater localized departures

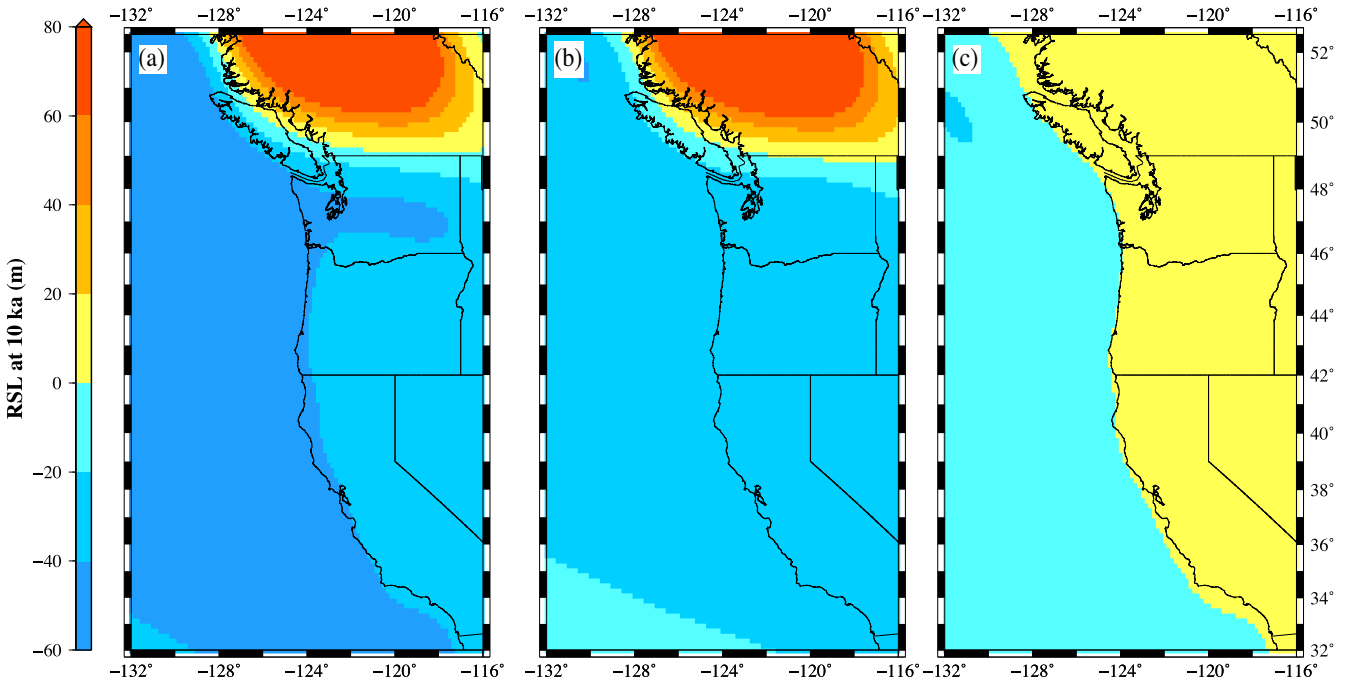

Figure 6. (a) Modelled RSL for the 1-D reference model (UMV = 2 $\times 10^{20}$ Pa s, LMV =10^{22} Pa s, and lithosphere thickness = 46 km) at 10 ka. The contribution to this signal from ice and ocean loads are plotted in (b) and (c), respectively. The results shown in (a) are not simply the sum of those in the other two plots due to the contributions from Earth rotation, meltwater addition (Barystatic sea level change) and syphoning which are included in (a) but not (b) or (c).

(>20 m) from the 1-D model are evident for all considered seismic models in northern Salish Sea.

Fig. 9 shows modelled RSL curves for the 1-D model case (UMV = 2 × 10^{20} Pa s, LMV =10^{22} Pa s and a constant lithosphere thickness of 46 km) along with results for the eight different realizations of lateral viscosity structure. We compute the modelled RSL curves at the average locations within each of the 13 sites as shown in Fig. 1 (black diamonds). The modelled RSL curves for sites in the northern region (sites 1–7) suggest a rapid RSL fall upon deglaciation followed by a gradual RSL rise during the early-to-mid Holocene and then relatively stable values towards the present time. In the central and southern regions, sites 8–13, results demonstrate persistent sea level rise throughout the Holocene reflecting the influence of peripheral bulge collapse as well as the addition of the meltwater to the oceans. As shown in Fig. 9 and described by Yousefi *et al.* (2018), the RSL curves based on an optimal 1-D viscosity model do not capture well the observed variability in RSL data across the study region and only provide relatively good fits at a subset of sites (6, 7, 8 and 11). However, the SLIPs from sites 6 and 11 are younger than ∼4 ka and so a broader range of 1-D viscosity models can adequately fit the data from these sites (Yousefi *et al.* 2018).

Adding lateral variations in viscosity structure results in a spread of the modelled curves (Fig. 9) that generally diminishes with distance from the northern region. Prior to ∼10 ka, RSL curves in the northern Salish Sea (site 3) show the greatest spread (more than 40 m) which reflects the results presented in Fig. 8 and Fig. S3. On the other hand, sites in the southern region (11–13) show the least spread (around 10 m or so). Over the mid-late Holocene, model curves for the central region (sites 8–10) demonstrate a relatively large range in RSL that is similar to that at northern sites (∼10–15 m). This is due to the S40RTS seismic model which produces notably higher RSL values in southern Washington and northern Oregon. One potential reason for these anomalously high RSL values is the existence of lower viscosity values in the mantle for this model compared to the three others considered (Fig. 3). However, a comparison of regional sub-lithosphere viscosity structure between all four seismic models (Fig. S4) indicates significant variability among different models which makes the interpretations of the RSL differences non-trivial.

A visual assessment on the data-model misfits in Fig. 9 reveals that the addition of lateral structure can improve the fit at a small number of sites, for example see the SMUCB model curve in northern Oregon (site 9) and central California (site 12). However, results at most sites seem to be relatively similar to that of the 1-D case, or, in some locations such as sites 3 and 8, the 1-D model provides the best fit to the data. All of the models struggle to capture the rapid RSL fall immediately after deglaciation, especially at sites 2, 3 and 5. One part explanation for this is the presence of higher viscosity values beneath this area (Fig S4) which is, in general, at least one order of magnitude greater than the proposed range in previous studies, that is UMV: 5 $\times 10^{18}$– 5 $\times 10^{19}$ Pa s, LMV: 1–3 $\times 10^{21}$ Pa s (James *et al.* 2000, 2009a,b; Yousefi *et al.* 2018). The other potential reason for this observed discrepancy is inaccuracy in the adopted ice model, which will be discussed in Section 4.

In order to examine whether there is a statistical preference between the eight different 3-D viscosity models considered, we calculate the data-model misfits using the following criterion (Mitrovica *et al.* 2000):

$$\delta = \frac{1}{N}\sqrt{\sum_{i=1}^{N}\left(\frac{RSL_i^{\text{obs}} - RSL_i^{\text{model}}}{\sigma_{rsl,i}}\right)^2 + \left(\frac{t_i^{\text{obs}} - t_i^{\text{model}}}{\sigma_{t,i}}\right)^2}, \quad (4)$$

where RSL_i^{obs} and RSL_i^{model} are the observed and predicted RSL values for the ith SLIP with observational uncertainty of $\sigma_{rsl,i}$; t_i^{obs}

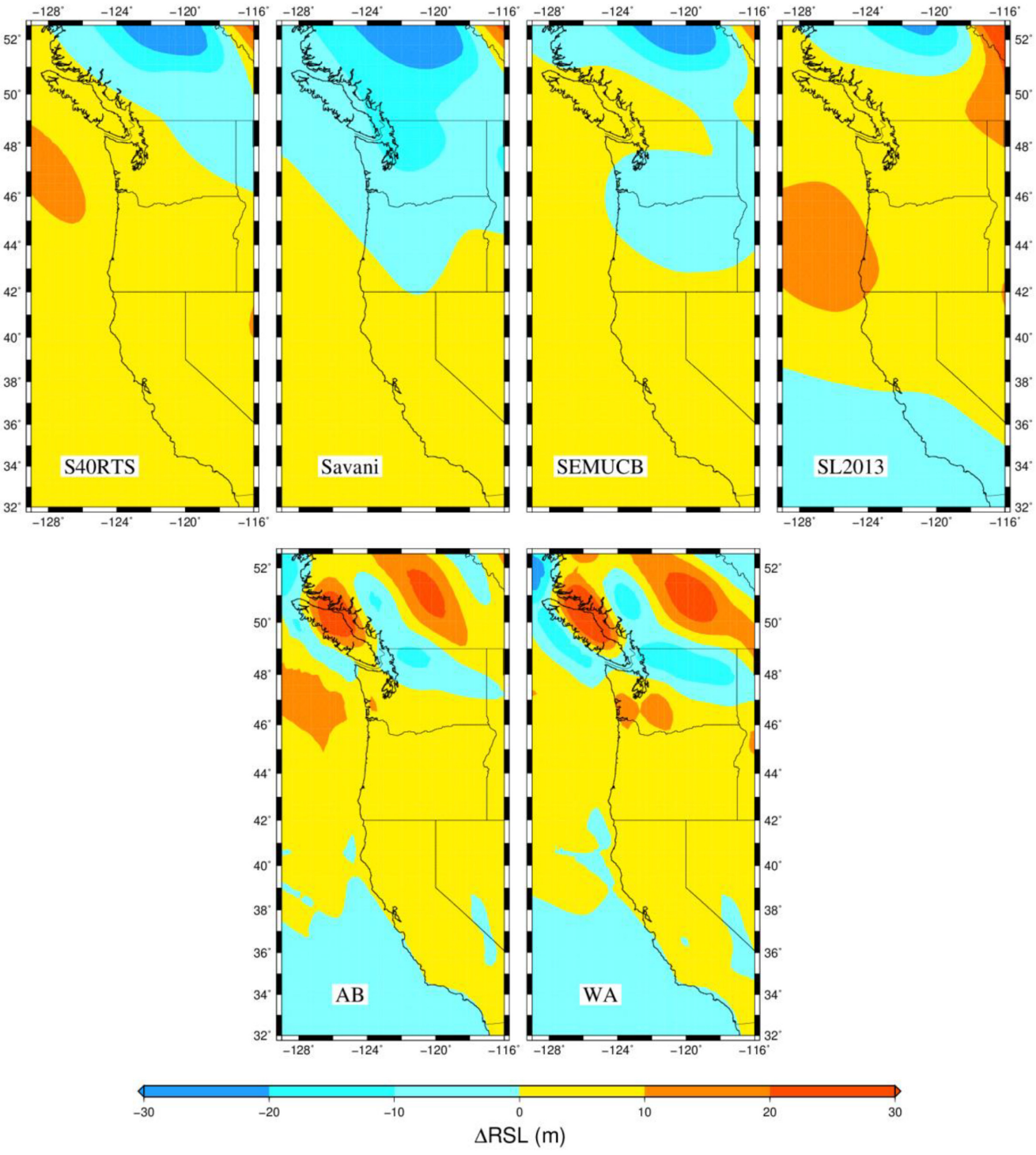

Figure 7. Modelled RSL changes compared to results for the reference 1-D viscosity model at 10 ka (Fig. 6a) when adding (top panel) lateral sublithosphere viscosity structure and (bottom panel) lateral variability in lithosphere thickness. All plots show 3-D model results minus those for the reference 1-D viscosity model.

and t_i^{model} are the observed and predicted age values with observational uncertainty of $\sigma_{t,i}$; and N is the total number of SLIPs. Note that the model values (t_i^{model}, RSL_i^{model}) are chosen such that the distance from the model curve to a given observation point is minimized (Mitrovica *et al.* 2000; Yousefi *et al.* 2018). Since data from the northern region are more challenging to fit, we also provide the misfit value when considering only the northern sites. A comparison between the misfit values suggests a small preference for the AB lithosphere model over the WA model (Fig. 10a). This preference is more evident when comparing values obtained for northern data only (Fig. 10b), which is also apparent from the model curves shown in Fig. 9 (solid lines versus dashed lines). The calculated

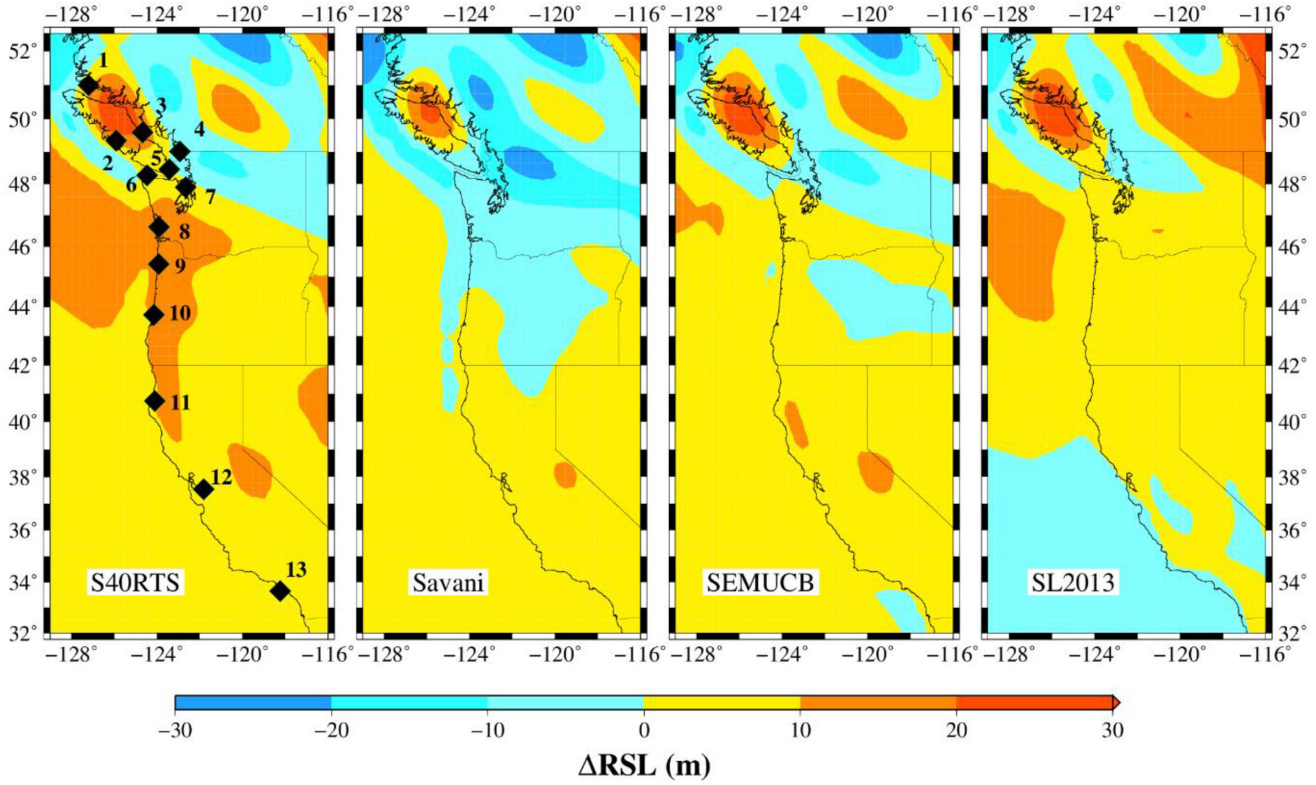

Figure 8. Modelled RSL changes compared to results for the reference 1-D viscosity model at 10 ka (Fig. 6a) when considering the combined effect of the lateral sublithosphere structure and elastic lithosphere thickness from the AB model. All plots show 3-D model results minus those for the reference 1-D viscosity model. The black diamonds indicate the average locations of the RSL data for each specific region. The RSL curves shown in Fig. 9 are computed at these locations.

misfits based on the entire data set do not reveal any clear preference for one of the seismic models. However, the WA-S40RTS model results in slightly larger misfit values than the other models which likely reflects the RSL curves for this model being considerably higher for central sites (8–10, Fig. 9). On the other hand, misfit values calculated using the observations from the northern region indicate that the AB-S40RTS model provides the best fit to these data. Overall, the results indicate that the eight realizations of lateral structure described above do not significantly improve the model fits relative to a 1-D model optimized to fit data from the central region.

3.2 3-D regional earth models

In this section, we consider the results from two different approaches, as described in Section 2.2.3, that capture the regional viscosity structure more accurately than the global seismic models. In Section 3.2.1 we present the results obtained from integrating a regional seismic tomography model within two of the global models. In Section 3.2.2, we investigate the sensitivity of the model output when considering subduction zone geometry and plate boundary locations to define 3-D viscosity structure.

3.2.1 Seismic inference

Fig. 11 represents the spatial variation in RSL at 10 ka relative to the 1-D reference model associated with the two models generated by insertion of a regional seismic model (Hawley & Allen 2019) into the global S40RTS and SEMUCB seismic models. The lateral variability in lithosphere thickness is adopted from the AB model in both cases. The results suggest that the RSL anomalies have a similar order of amplitude to those obtained from the global models (compare Fig. 11 with Fig. 8) with maximum RSL differences compared to the 1-D reference model of ∼30 m in northcentral Vancouver Island which is mainly governed by lateral variations in lithosphere structure. The longer wavelength signals of the regional model also follow a relatively similar pattern to those of the corresponding (background) global models with positive RSL departures along most parts of the coast south of Puget Sound. In order to highlight the influence of the higher-resolution viscosity structure from the regional seismic model, the difference between the RSL model outputs from the integrated models and the global models (Fig. 8) is plotted in Fig. 11(right-panel plots). These differences for the regional model embedded within the S40RTS model are generally small and in the range of ±2 m along the majority of the coastline but with larger deviations in Puget Sound. The negative RSL anomalies in the Puget Sound area and northern California are likely due to the higher-viscosity structure of the subducting slab. The positive RSL departures that appear between ∼42°N and ∼45°N, which are more apparent in the SEMUCB case, might reflect the combined effect of the slab hole and the reduced viscosities of the mantle wedge (Fig. 4, Figs S2 and S5). Results for the SEMUCB model produce larger deviations (±4–10 m) in the northern and central region, particularly in southeastern Georgia Strait in the Salish Sea (site 4) and Oregon State (sites 8–10). Due to the proximity of the loading centre in the north to the boundary zone over which the regional model is patched into the global model, some of the deviations at site 4 are likely the result of the regional model integration process described in Section 2.2.3.

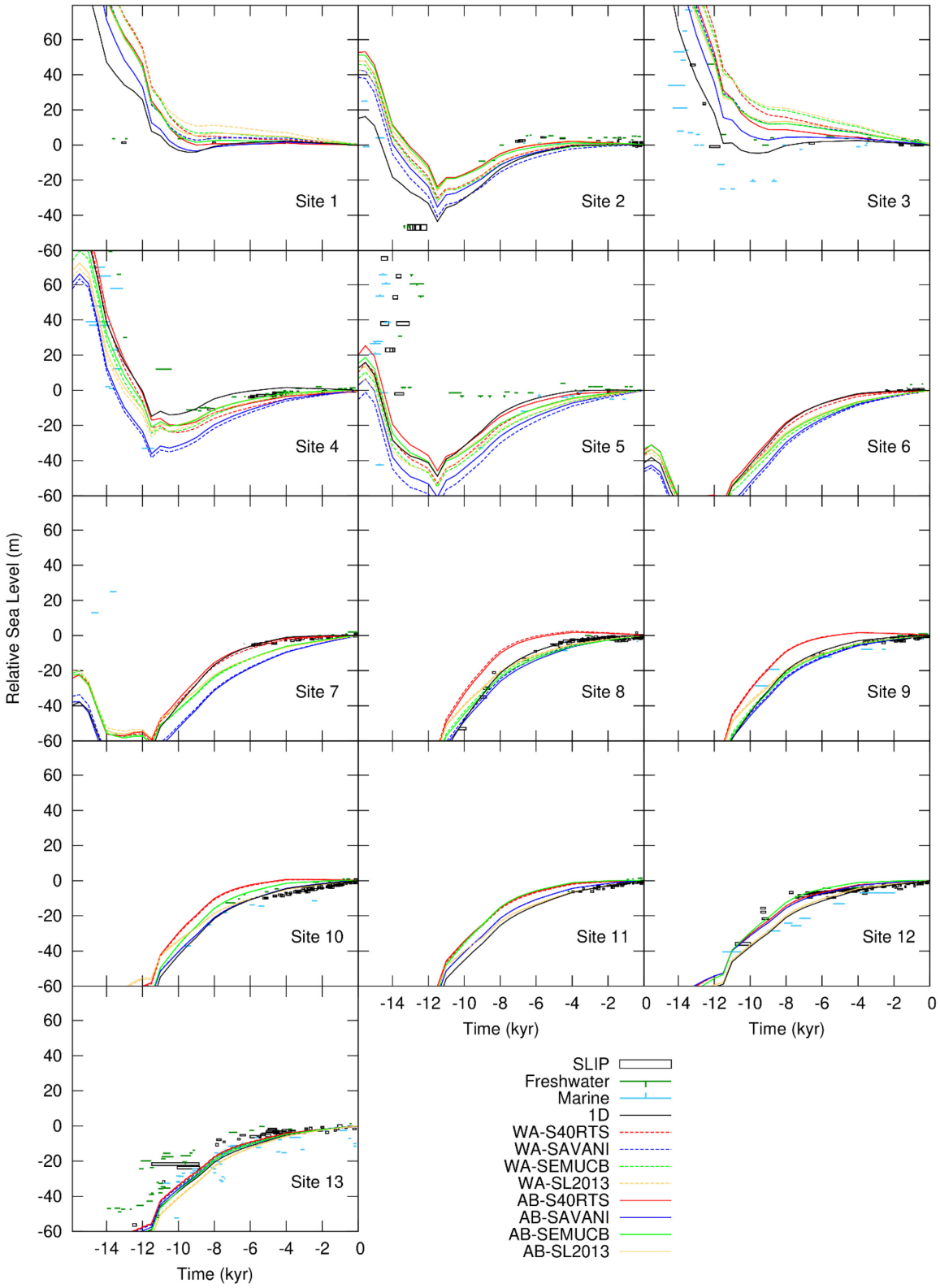

Figure 9. RSL data-model comparison for eight realizations of lateral viscosity structure (based on two models of lithosphere thickness and four global seismic models) at the 13 sites shown in Fig. 8 (black diamonds). RSL curves for the 1-D reference viscosity model are shown by the black lines. The SLIP boxes represent 1σ uncertainty in height and age. The meaning of each data symbol and the 3-D viscosity model represented by each curve are indicated in the key.

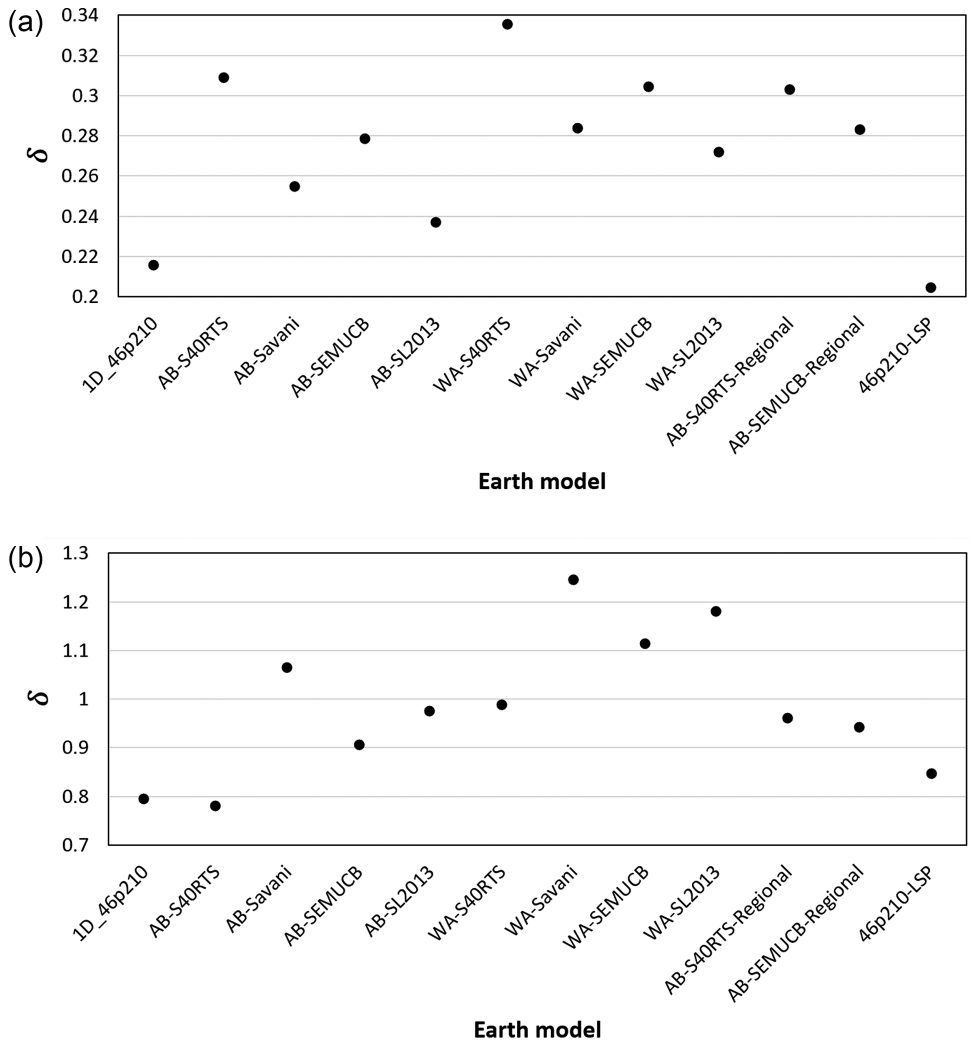

Figure 10. Data-model misfit values calculated based on: (a) the entire data set; and (b) data from the northern region only.

Fig. 12 illustrates the model RSL curves for the seismically inferred regional structure embedded within the two global models at the average locations of our 13 sites. The RSL curves associated with the S40RTS and SEMUCB seismic models are also shown in the same plot. The departure of the regional RSL curves from the 1-D model follow closely the corresponding global model curves with some notable differences in northern and central sites. The central sites are particularly affected for the case with SEMUCB as background due to the amplified influence of the slab hole and relatively lower viscosities in the mantle wedge as stated above. The calculated data-model misfit values (Fig. 10) do not indicate preference of the 3-D regional models over the 1-D case or the global models. The inclusion of the high-resolution regional structure produces larger misfits than the background global models when considering the data from the northern region which is consistent with the increased misfit observed for sites 4, 5 and 7 in Fig. 12.

3.2.2 Slab and mantle wedge model

Fig. 13 shows modelled RSL at 10 ka relative to the 1-D reference model for four different 3-D cases that consider the: (1) mantle wedge low-viscosity zone (LVZ) only; (2) slab only; (3) LVZ and slab and (4) LVZ, slab and plate boundary. We note that considering the mantle wedge and slab in isolation is not realistic given that they most likely co-exist and the presence of each will impact the deformational response of the other (particularly the slab on the LVZ; e.g. Suito & Freymueller 2009). The results in Fig. 13 show that our estimates of this regional structure cause smaller RSL variations, with a peak of ∼15 m, in comparison to the 3-D structure inferred from global and regional seismic models. According to Fig. 13(a), the low-viscosity layer has a small effect (less than a few meters in amplitude) that could be due to its position relative to the ice loading. This low sensitivity to the LVZ is quite surprising, since a numerical experiment of the glacial isostatic response at the southern Chile subduction zone suggested that the presence of a low-viscosity wedge enhances the modelled displacement field over a region that extends beyond that immediately above the LVZ (Klemann *et al.* 2007). The authors attribute this wide-ranging effect of the LVZ to the loading induced flux of the wedge material which is dependent on the slab length and geometry. However, they also indicate that the influence of the LVZ in amplifying the deformation field depends strongly on the location of the wedge which, in their case, is located directly beneath the loading (Klemann *et al.* 2007).

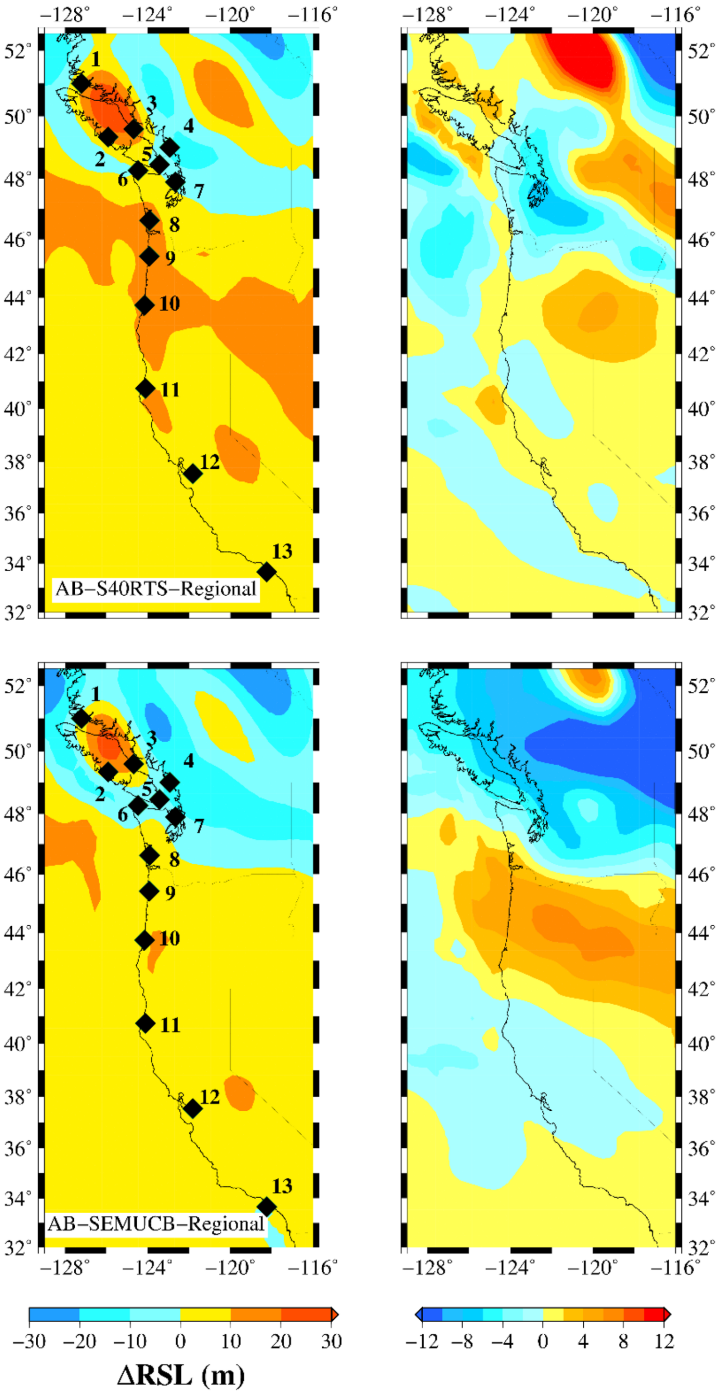

Figure 11. Left-hand panel: modelled RSL changes relative to the reference 1-D viscosity model at 10 ka for the viscosity structure inferred from a regional seismic velocity model (Hawley & Allen 2019) integrated with the (top panel) S40RTS, and (bottom panel) SEMUCB global velocity models. Right-hand panel: the difference between these integrated models with the results inferred from the associated global models as shown in Fig. 8. The elastic lithosphere thickness considered in both cases is the AB model. The black diamonds indicate the average locations of the RSL data distribution shown in Fig. 1. The RSL curves shown in Fig. 12 are computed at these locations.

The slab structure has a greater impact on the RSL variations (Fig. 13b) reaching a maximum (∼15 m) at the northern tip of Vancouver Island and Puget Sound; the latter being located just off the northern edge of the slab. The influence of the slab structure on RSL can be explained by the damping effect of the higher viscosity slab on both the isostatic rebound and the peripheral bulge collapse which cause positive and negative RSL signals, respectively, with respect to the reference model (Fig. 5a). The combined effect of the LVZ and the slab (Fig. 13c) is dominated by the slab structure so that the influence of the LVZ is not visually distinguishable from the case of including the slab only.

The addition of a plate boundary that acts as a weak zone in the lithosphere results in a RSL signal with an amplitude of several metres that tracks the locations of these weak zones (Fig. 13d).

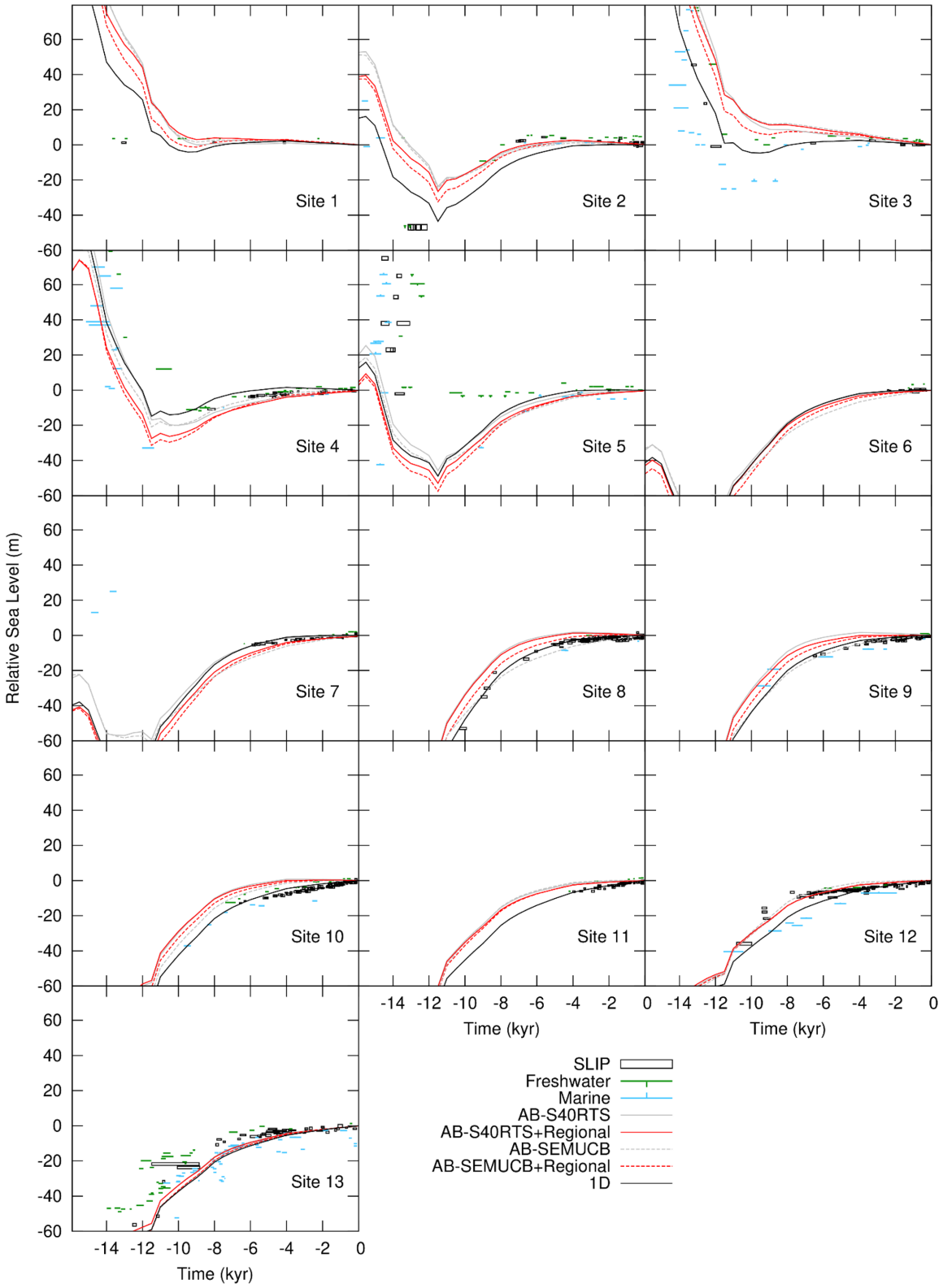

Figure 12. RSL data-model comparison for the higher-resolution regional viscosity model embedded within the S40RTS model (solid red line) and the SEMUCB model (dashed red line). The RSL models corresponding to the S40RTS and SEMUCB global models are shown as the grey solid and dashed lines, respectively. RSL for the 1-D reference viscosity is shown by the black line. The AB lithosphere thickness model was used for all results plotted in this figure. The SLIP boxes represent 1σ uncertainty in height and age. The meaning of each data symbol and the 3-D viscosity model represented by each curve are indicated in the key.

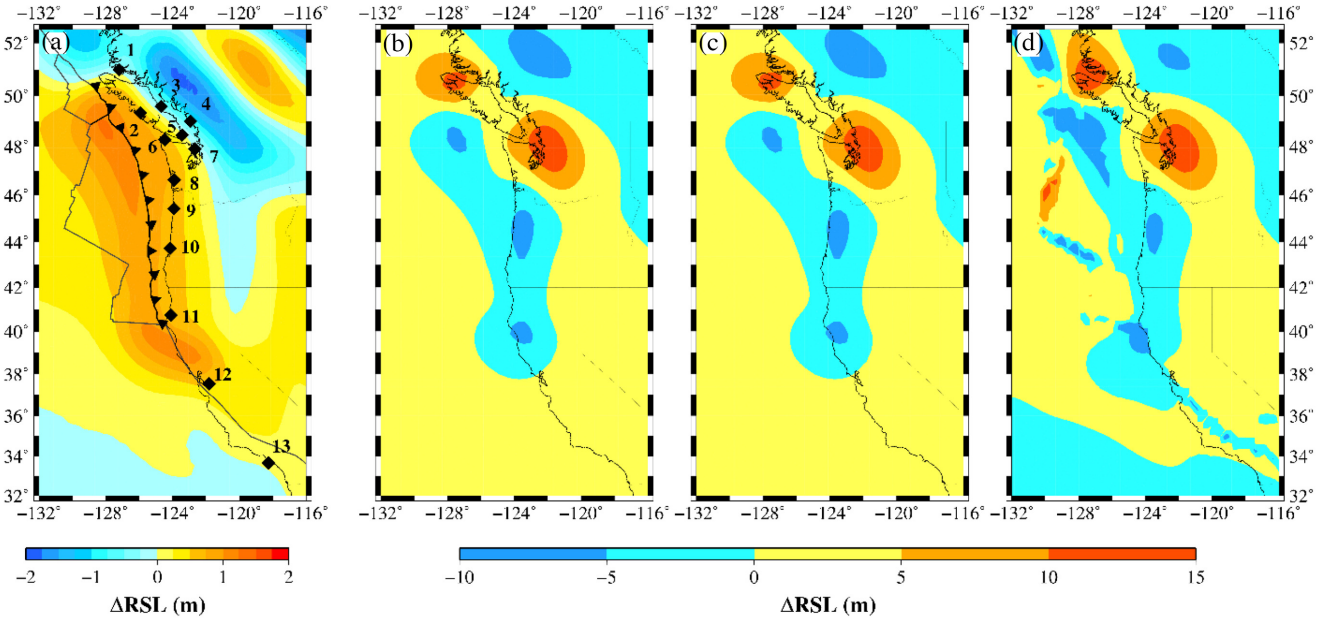

Figure 13. Modelled RSL changes relative to the 1-D reference model at 10 ka when considering regional tectonic structure of the Cascadia subduction zone and its vicinity: (a) mantle wedge LVZ only; (b) subducting slab only; (c) LVZ plus slab and (d) LVZ plus slab and plate boundary. The black diamonds indicate the average locations of the RSL data distribution shown in Fig. 1. The RSL curves shown in Fig. 14 are computed at these locations.

Since no tectonic stresses nor plate motions are considered, the RSL signal associated with the inclusion of plate boundaries reflects deformation associated with GIA-related stresses only (ice/ocean loading and change in the rotational potential). Horizontal stresses likely dominate the signal associated with these zones (e.g. Latychev *et al.* 2005b) with areas showing negative RSL values being characterized by subsidence of these areas relative to the 1-D reference simulation (the opposite being true for areas showing a positive RSL signal). A more robust interpretation of these features requires consideration of the stress field evolution in these regions.

We performed an additional simulation by decreasing the slab viscosity by three orders of magnitude (10^{23} Pa s). The resulting perturbations on RSL predictions at 10 ka compared to the results in Fig. 13(d) is less than ± 1 m (Fig. S6). We also performed a sensitivity analysis to assess the effect of reducing the mantle wedge viscosity from 10^{18} to 10^{15} Pa s and no significant difference was observed.

In Fig. 14 we evaluate the effect of the 3-D structure shown in Fig. 5 on the temporal variation of RSL at our 13 sites. The results show that RSL sensitivity to the regional structure varies from site to site. The largest differences (relative to the 1-D model results) occur prior to 10 ka and (mostly) in the northern region, particularly in Queen Charlotte strait and Puget Sound (sites 1 and 7). On the other hand, southern Washington (site 8), central and southern California (sites 12 and 13) indicate low sensitivity to this realization of lateral viscosity structure.

A comparison between the model curves in Fig. 14 reveals that adding this realization of lateral structure results in no clear improvement in the data-model misfits, other than in central Oregon (site 10). When considering the misfit value calculated using the entire data set (Fig. 10a), the 3-D model considered in this section gives the best result (lowest misfit) compared to other 3-D models considered above with a misfit value that is very similar to that obtained for the 1-D reference model.

4 GENERAL DISCUSSION

In this section, we try to address some of the possible reasons behind the data-model discrepancies which can motivate future work. According to the calculated misfit values (Fig. 10), the application of different realizations of 3-D Earth viscosity structure does not considerably improve the data-model fits compared to the 1-D case. Only the slab and mantle wedge model generates slightly better fits to the data set and this largely reflects the relatively minor influence of this Earth structure on the computed RSL values for this case. Overall, our results do not indicate a strong statistical preference for a particular seismic model or preference of the regional model over the global models. However, of the four global seismic models considered, SL2013 is preferred when all data are considered regardless of the adopted lithosphere model. Another noteworthy result is that the AB lithosphere model produces lower misfits than the WA model for all (sublithosphere) viscosity models. When considering only the northern sites, where all models struggle to fit the deglacial RSL fall, the AB-S40RTS provides the optimum fit. On the other hand, this model results in the highest misfit values when all observations are considered. Therefore, the results of our analysis indicate that lateral viscosity structure does not appear to be the primary source of the data-model fits in the northern region. This conclusion is the primary motivation for the following discussion.

The uncertainty in the model results reflects our incomplete knowledge of both the applied Earth model and ice loading history. Although there is insufficient data to completely resolve this ambiguity and ensure a unique GIA solution, there are some approaches that can reduce sensitivity to one of these two model inputs so that the other can be more robustly determined. Two such approaches are restricted to the application of RSL observations in either near-field regions, close to the centre of the ice loading (Mitrovica & Peltier 1993), or far-field regions, distant from major glaciation centres (Nakada & Lambeck 1989), and thus not applicable here. However, performing a sensitivity analysis by exploring a large parameter space enables us to assess the relative importance

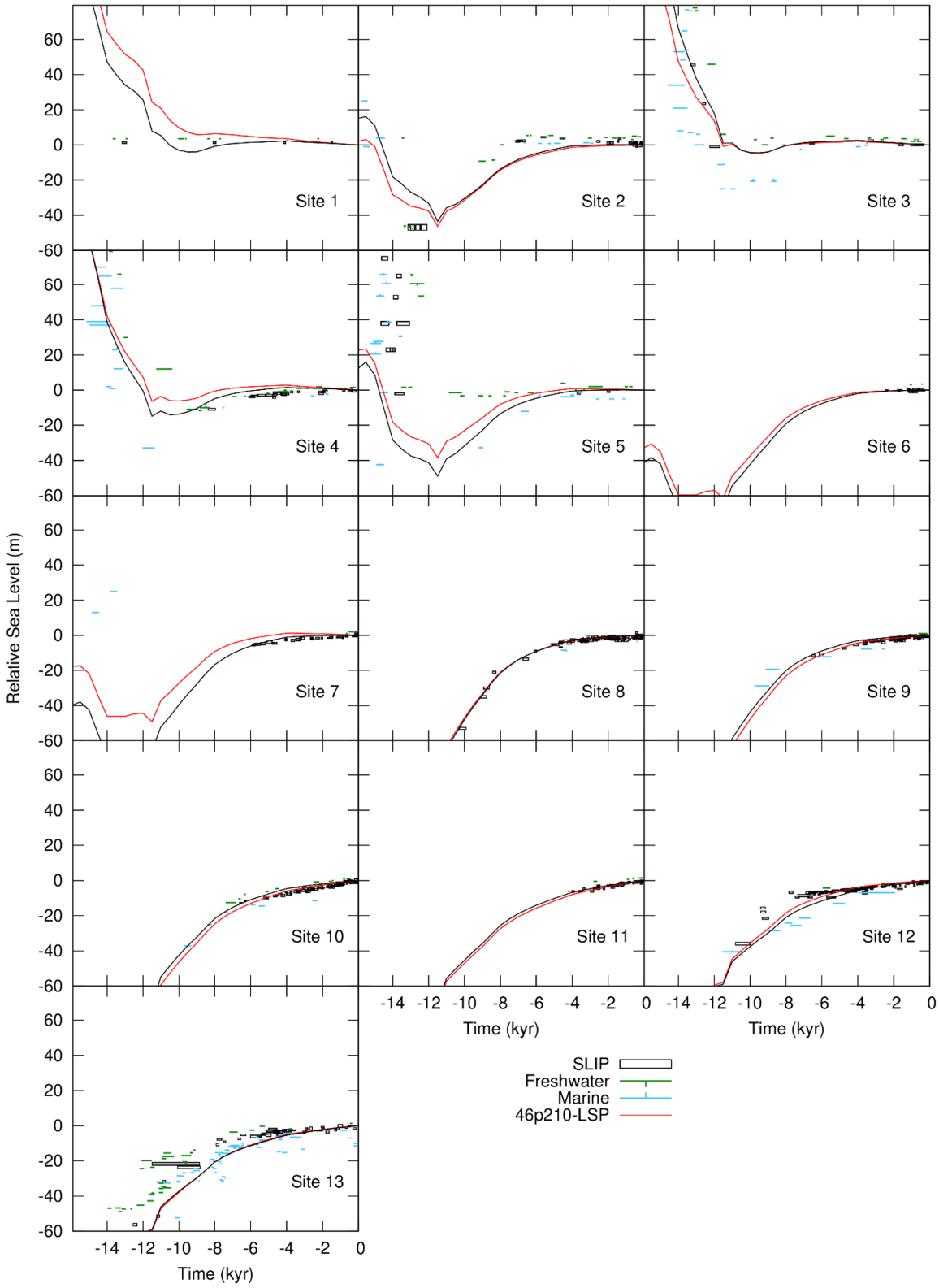

Figure 14. RSL data-model comparison for a 3-D viscosity model (red line) based on the regional tectonic structure of the Cascadia subduction zone and immediate vicinity, that is LVZ plus the subducting slab and the plate boundary. RSL for the 1-D reference viscosity is shown as a solid black line.

of each component. In the 1-D GIA study of Yousefi *et al.* (2018), more than 20 000 model runs were performed to find an optimal set of parameters that best fits the regional RSL data set. Their results indicate that the contribution from the ice model becomes particularly important for those sites located in northern Cascadia, as they show high sensitivity to differences in the applied ice model (see their Fig. 5). One example of this sensitivity is the rapid fall of RSL from the high-stand elevation of >70 m around 14 ka recorded

at southern Vancouver Island (site 5), which cannot be reproduced with the model curves shown in Fig. 9.

Yousefi *et al.* (2018) applied different ice models with deglaciation delayed by 500 and 1000 yr and showed that a model with a 500-yr delay (red curve in Fig. S7) best fits the observations from northern sites. However, the only model that can capture the oldest high-stand sea level at site 5 is that produced by delaying the deglaciation chronology by 1000 yr combined with an upper mantle viscosity that is two orders of magnitude lower than our reference model (blue curve in Fig. S7). In order to emphasize the importance of an accurate ice loading history, a model curve is also plotted based on this lower viscosity earth model and a 500-yr delay in deglaciation (green curve in Fig. S7). A comparison between these model results indicates that delaying the deglaciation by ∼1000 yr is necessary to adequately reproduce the rapid RSL fall at site 5 with an amplitude that matches the observations. This delayed deglaciation is also compatible with SLIPs at site 3.

The ice model that is used in this study (#6885) is selected from a larger ensemble of reconstructed deglacial histories of the North American ice complex (Tarasov *et al.* 2012), which have been calibrated with the radiocarbon data set of Dyke *et al.* (2003) and Dyke (2004). The ice margin extent of our model shows good agreement with these observational constraints which suggest that the southeastern tip of Vancouver Island became ice free after 15 ka (Fig. S8, see also Gowan 2007). However, given that there is limited dating control on the ice margin chronology during the initial stages of deglaciation, the isochrons have relatively large temporal uncertainty (∼±1000 yr, Dalton *et al.* 2020), and so one cannot rule out the possibility of delaying the retreat of our ice model from the Victoria region by 500–1000 yr. The source of this uncertainty in defining the ice chronology can be attributed to: the limited available radiocarbon ages (Dalton *et al.* 2020), uncertainties associated with radiocarbon dating and calibration (Törnqvist *et al.* 2015), and relating these calibrated dates to the actual pattern of ice retreat (Tarasov *et al.* 2012). This uncertainty and the importance of the ice history in computing RSL curves in southern British Columbia emphasizes the need for improved chronological constraints on the early deglacial history in this region. This can be partly fulfilled with acquisition and incorporation of additional radiocarbon data as well as the application of alternative dating methods such as ^{10}Be (Ullman *et al.* 2016; Darvill *et al.* 2018).

A previous GIA study of northern Cascadia by James *et al.* (2009) showed that including a low-viscosity asthenosphere layer can replicate the rapid RSL fall in the Victoria region. Based on the results in this study and those of Yousefi *et al.* (2018), we conclude that the ability of the GIA model in James *et al.* (2009) to fit the observations is mainly the result of their applied ice sheet reconstruction rather than the applied earth model. Our conclusion is based on the fact that James *et al.* (2009a,b) modified both the amplitude and the timing of deglaciation to fit the rapid sea level fall in Victoria region. Their ice model features ∼2150 m of ice in the southeastern tip of Vancouver Island during its maximum extent at 15.4 ka. Our ice model, in contrast, reaches a maximum thickness of ∼1000 m at ∼16–17 ka which had reduced to ∼500 m by 15.4 ka. Further work is required to determine which of these two model reconstructions is more accurate.

Assuming our applied ice model is fairly accurate in terms of deglaciation amplitude, the inability of the above 3-D Earth modelling to generate the observed RSL fall in the Victoria region suggests that the mantle viscosity inferred using the global and regional seismic models is not low enough in this region (Figs S4 and S5). A key source of uncertainty in estimating lateral viscosity structure is related to the scaling between seismic velocity and viscosity (e.g. Forte & Mitrovica 2001; Wu *et al.* 2013). As an example, Clark *et al.* (2019) performed a sensitivity analysis that focused on this scaling by exploring ϵ values (see eq. 3 in Section 2.2.2) in the range 0.005–0.04 which can cause the range in viscosity perturbations to vary by ∼3.5 orders of magnitude. Although they applied only one global seismic model (S40RTS), their results indicate significant influence of uncertainty associated with this parameter on the predicted RSL curves. Better quantifying this scaling uncertainty and considering additional data sets and methods to reduce it is an important target for future work. A recent study by Li *et al.* (2020) aimed to quantify the Earth-model-related uncertainty in GIA model results by applying different realizations of 3-D viscosity structure. We note that our results show greater sensitivity to different realizations of lateral structure, particularly within the lithosphere (e.g. compare our Fig. S9 with fig. S12a in Li *et al.* 2020). This is likely related to the spatial resolution of the GIA models and the different methods used to determine viscosity structure. However, this indicates that a spatial resolution of ∼10 km (as opposed to ∼50 km in the Li *et al.* model) is required to accurately simulate the influence of lateral structure in our study region.

In our analysis, we assume that the seismic velocity anomalies and the viscosity variations are driven by temperature only. Several studies indicate that there can be significant contributions from heterogeneity in chemical composition and partial melting (Wang *et al.* 2008; Wu *et al.* 2013; Li *et al.* 2018). Separating the effect of each individual factor is not straightforward and requires complementary constraints such as seismic wave attenuation, electrical conductivity, heat flow, and density (Karato 2008; Dalton *et al.* 2009) and/or applying a joint inversion of seismic and other geodynamic observables (Afonso *et al.* 2016, 2019). In this regard, interpretation of the seismic velocity and attenuation models together may help to better explain the role of each contributor to the variations in seismic velocity and subduction zone structure. For instance, a slower seismic velocity joint with high attenuation can be attributed to elevated temperatures and the presence of melt or increased water content (Dalton *et al.* 2009). The estimated *S*-wave attenuation in coastal areas of western North America suggests that there are considerable variations in seismic attenuation along the coastline indicating higher values in southern Oregon and north–northwestern Washington (e.g. Eilon & Abers 2017). Along with these high attenuation values, several tomographic studies feature low seismic velocity anomalies beneath these areas (Hawley *et al.* 2016; Bodmer *et al.* 2018; Hawley & Allen 2019). Bodmer *et al.* (2018) argue that the dominant controlling mechanism of the subslab mantle structure in northern Cascadia is the nearby oceanic hot spot, however, the observed low velocity in this region cannot be entirely due to temperature variations. They propose that decompression melting is also at play in this region and, more importantly, in southern Cascadia as a result of rapid motion of the Pacific Plate relative to the Gorda deformation zone which promotes mantle upwelling. These results provide an explanation as to why our estimates for viscosity in this region appear to be biased high.

Part of the uncertainty in developing the lateral viscosity structure is associated with the applied seismic velocity model. Although the regional tomographic model used here is generally compatible with the other models, there are some inconsistencies. One example is the margin-wide, subslab low velocity zone featured in the model of Hawley & Allen (2019); there is a debate regarding the spatial continuity of this low velocity anomaly with some results suggesting it is not continuous but localized to northern (>46°N) and southern

(<43°N) Cascadia (Bodmer *et al.* 2018). A similar along-strike heterogeneity has been proposed for the shallower (<80 km) structure of the forearc mantle (Delph *et al.* 2018). Regarding the relatively young age of the subducting plates (∼ 4–9 Myr), it is still an open discussion as to whether the apparent trench-parallel variations in seismic velocity originate from thermal structure and the subsequent changes in slab hydration state or variations in the permeability of the down-going slab (Delph *et al.* 2018).

In simulating Earth deformation, we consider a Maxwell steady-state rheology where the relation between stress and strain rate is linear. There is the possibility that the behaviour of the mantle follows a power-law deformation where lower effective viscosity values are induced by the high stress levels upon the onset of the deglaciation and the viscosity increases with stress reduction (e.g. Wu & Wang 2008; James *et al*. 2009a,b). In contrast to these assumptions of a purely linear or purely non-linear rheology for mantle material, an alternative hypothesis suggests that both linear diffusion creep and non-linear dislocation creep operate simultaneously in the mantle, the so called 'composite rheology'. Some recent applications of earth models with composite rheology show promising results and improvement in fitting observational constraints (van der Wal *et al.* 2013, 2015; Huang *et al.* 2019). Another possible departure from a Maxwell rheology is the existence of a transient response as evident in the more general Burgers rheology, where the apparent viscosity is less than that of the steady state deformation during periods of rapid changes in driving stress (Ranalli 1998). The more rapid deformational response that is characteristic of these more complex models might be necessary to accurately capture the large and rapid signal evidence in the northern RSL observations.

An additional limitation of our assumed rheological model is that brittle failure is not simulated. Studies have shown that faults can be reactivated during periods of rapid ice thinning resulting in large surface displacements (e.g. Arvidsson 1996; Steffen *et al.* 2020). The Victoria region is located near the Leech River-Devil's mountain fault system that appears to have ruptured during the Holocene (Morell *et al.* 2017, 2018; Barrie & Greene 2018). Further investigations are warranted to support or refute the possible influence of fault rupture on RSL changes during and following the Late Glacial period.

5 CONCLUSIONS

In this study, we examined the influence of lateral Earth structure on GIA model results along the west coast of North America. We developed eight different realizations of laterally variable viscous Earth structure based on four global seismic velocity models and two global lithosphere thickness models. The results from these 3-D models were compared to those derived from a reference 1-D model with UMV $= 2 \times 10^{20}$ Pa s, LMV $= 10^{22}$ Pa s, and a lithosphere thickness of 46 km.

The effect of lateral variations in sublithosphere mantle viscosity on RSL output varies from one seismic model to another but generally lies within ±10 m relative to the 1-D background model results. The variability in lithosphere structure causes localized higher amplitude changes with a spatial pattern that is similar for the two lithosphere models considered here. The combined effect of the sublithosphere viscosity variations and laterally variable lithosphere structure causes less than ±20 m RSL changes along the coastline from northern Washington coast to southern California at 10 ka. These departures from the reference 1-D model results are largest in the northern region, particularly in the northern Salish Sea, where the influence of lateral structure reaches ∼30 m at this time. RSL data-model comparison does not reveal a clear preference of any particular seismic model or significant improvement in model misfits compared to the 1-D reference viscosity model. However, our results do suggest a weak but consistent preference for the AB lithosphere model.

Given the lack of spatial resolution in the global seismic models, we also considered two different approaches to better resolve regional lateral structure associated with the Cascadia subduction zone: one based on a regional seismic model and the other using constraints on slab geometry. Regardless of the approach taken, the results indicate that the influence of the subducting slab has the greatest impact on RSL simulation with a peak amplitude of ∼15 m in the northern tip of Vancouver Island and Puget Sound. In contrast, the results show little sensitivity to the existence of a postulated low-viscosity mantle wedge, with an RSL signal less than a few meters. We postulate that this low sensitivity is due to either its position with respect to the ice loading and/or its relatively small volume.

The different realizations of 3-D viscosity structure considered in this study do not significantly improve the data-model misfits compared to results using a 1-D viscosity model, particularly at sites located in northern Cascadia, where all of the models struggle to capture the amplitude of rapid RSL fall during deglaciation. The different 3-D earth models applied in this study give insight into the influence of lateral viscosity structure, which is a necessary step towards estimating GIA model uncertainty. Overall, our results indicate that future studies should focus on developing a more accurate ice model before further attempts are made to improve the Earth component of the GIA model via better constraints on 3-D Earth structure and/or applying more complex rheological models.

ACKNOWLEDGEMENTS

We thank Jeffrey Freymueller and an anonymous reviewer for their constructive reviews. We acknowledge Thomas James, Giorgio Ranalli, Pascal Audet and Claire Perry for input related to a draft version of this manuscript. We also thank Lev Tarasov for providing ice models and discussing the chronological constraints. Funding support was provided by the Natural Sciences and Engineering Research Council of Canada, and the University of Ottawa. This paper is a contribution to the PALSEA working group.The results presented here benefitted from feedback and discussions at the SERCE/SCAR GIA workshop, Ottawa, 2019. Model results produced in this study using 3D Earth structures (relative sea level curves and present-day vertical land motion rates) are available through Mendeley Data (https://data.mendeley.com/datasets/svz3d99tmm/1).

REFERENCES

Afonso, J.C., Rawlinson, N., Yang, Y., Schutt, D.L., Jones, A.G., Fullea, J. & Griffin, W.L., 2016. 3D multiobservable probabilistic inversion for the compositional and thermal structure of the lithosphere and upper mantle: III. Thermochemical tomography in the Western-Central US, *J. geophys. Res.,* **121**(10), 7337–7370.

Afonso, J.C., Salajegheh, F., Szwillus, W., Ebbing, J. & Gaina, C., 2019. A global reference model of the lithosphere and upper mantle from joint inversion and analysis of multiple data sets, *Geophys. J. Int.,* **217,** 1602–1628.

Ahren, J., Geveci, B. & Law, C., 2005. ParaView: An End-User Tool for Large Data Visualization, *The Visualization Handbook,*ISBN-13: 978-0123875822.

Arvidsson, R., 1996. Fennoscandian earthquakes: Whole crustal rupturing related to postglacial rebound, *Science,* **274,** 744–746.
Audet, P. & Burgmann, R., 2011. Dominant role of tectonic inheritance in supercontinent cycles, *Nat. Geosci.,* **4,** 184–187.
Auer, L., Boschi, L., Becker, T.W., Nissen-Meyer, T. & Giardini, D., 2014. Savani: a variable resolution whole-mantle model of anisotropic shear velocity variations based on multiple data sets, *J. geophys. Res.,* **119,** 3006–3034.
Austermann, J., Mitrovica, J.X., Latychev, C. & Milne, G.A., 2013. Barbados based estimate of ice volume at last glacial maximum effected by subducted plate, *Nat. Geosci.,* **6,** 553–557.
Barrie, V. & Greene, H.G., 2018. An active Cascadia upper plate zone of deformation, Pacific Northwest of North America, *Sediment. Geol.,* **364,** 228–241.
Billen, MI., 2008. Modeling the dynamics of subducting slabs, *Ann. Rev. Earth planet. Sci.,* **36,** 325–356.
Bird, P., 2003. An updated digital model of plate boundaries, *Geochem. Geophys. Geosyst.,* **4,** Q1027, doi:10.1029/2001GC000252.
Blair, J.L., McCrory, P.A., Oppenheimer, D.H. & Waldhauser, F., 2011 revised (2013). A geo-referenced 3D model of the Juan de Fuca Slab and associated seismicity, U.S. Geological Survey Data Series 633, v.1.2, https://pubs.usgs.gov/ds/633/.
Bodmer, M., Toomey, D.R., Hooft, E.E.E. & Schmandt, B., 2018. Buoyant asthenosphere beneath Cascadia influences megathrust segmentation, *Geophys. Res. Lett.,* **45,** 6954–6962.
Brocher, T.M., Parsons, T., Tréhu, A.M., Crosson, R.S., Snelson, C.M. & Fisher, M.A., 2003. Seismic evidence for widespread serpentinized forearc upper mantle along the Cascadia Margin, *Geology,* **31,** 267–270.
Caldwell, J.G. & Turcotte, D.L., 1979. Dependence of the thickness of the elastic lithosphere on age, *J. geophys. Res.,* **84,** 7572–7576.
Chen, B., Haeger, C., Kaban, M.K. & Petrunin, A.G., 2017. Variations of the effective elastic thickness reveal tectonic fragmentation of the Antarctic lithosphere, *Tectonophysics,* **746,** 412–424.
Chopelas, A. & Boehler, R., 1992. Thermal expansivity in the lower mantle, *Geophys. Res. Lett,* **19,** 1983–1986.
Clague, J.J. & James, T.S., 2002. History and isostatic effects of the last ice sheet in southern British Columbia, *Quater. Sci. Rev.,* **21,** 71–87.
Clark, J., Mitrovica, J.X. & Latychev, K., 2019. Glacial isostatic adjustment in Central Cascadia: insights from three-dimensional Earth modeling, *Geology,* **47**(4), 295–298.
Clark, J.A., Ferrel, W.E. & Peltier, W.R., 1978. Global changes in postglacial sea level: a numerical calculation, *Quater. Res.,* **9,** 265–287.
Currie, C.A., Wang, K., Hyndman, R.D. & He, J., 2004. The thermal effects of steady-state slab-driven mantle flow above a subducting plate: the Cascadia subduction zone and backarc, *Earth planet. Sci. Lett.,* **223,** 35–48.
Dalton, A.S. *et al.* 2020. An updated radiocarbon-based ice margin chronology for the last deglaciation of the North American Ice Sheet Complex, *Quater. Sci. Rev*. **234,** 1–27.
Dalton, C.A., Ekström, G. & Dziewonski, A.M., 2009. Global seismological shear velocity and attenuation: a comparison with experimental observations, *Earth planet. Sci. Lett.,* **284,** 65–75.
Darvill, C.M., Menounos, B., Goehring, B.M., Lian, O.B. & Caffee, M.W., 2018. Retreat of the western Cordilleran Ice Sheet margin during the last deglaciation, *Geophys. Res. Lett.,* **45,** 9710–9720.
Delph, J.R., Levander, A. & Niu, F., 2018. Fluid controls on the heterogeneous seismic characteristics of the Cascadia margin, *Geophys. Res. Lett.,* **45**(20), 11 021–11 029.
Dyke, A.S., 2004. An outline of North American deglaciation with emphasis on central and northern Canada, in *Quaternary Glaciations-Extent and Chronology,* Part II, Vol. 2b, pp. 373–424, eds Ehlers, J. & Gibbard, P.L., Elsevier.
Dyke, A.S., Moore, A. & Robertson, L., 2003. Deglaciation of North America. Tech. Rep. Open File 1574, Geological Survey of Canada, Thirty-Two Maps at 1:7000000 Scale with Accompanying Digital Chronological Database and One Poster (in Two Sheets) with Full Map Series.
Dziewonski, A. & Anderson, D., 1981. Preliminary reference earth model, *Phys. Earth planet. Inter.,* **25,** 297–356.
Eilon, Z.C. & Abers, G.A., 2017. High seismic attenuation at a mid-ocean ridge reveals the distribution of deep melt, *Sci. Adv.,* **3**(May), e1602829, doi:10.1126/sciadv.1602829.
Engelhart, S.E., Vacchi, M., Horton, B.P., Nelson, A.R. & Kopp, R.E., 2015. A sea-level database for the Pacific coast of central North America, *Quater. Sci. Rev.,* **113**(0), 78–92.
Forte, A.M. & Mitrovica, J.X., 2001. Deep mantle high-viscosity flow and thermochemical structure inferred from seismic and geodynamic data, *Nature,* **410**(6832), 1049–1056.
Forte, A.M. & Woodward, R.L., 1997. Seismic-geodynamic constraints on three-dimensonal structure, vertical flow, and heat transfer in the mantle, *J. geophys. Res.,* **102,** 17 981–17 994.
Freelan, S., 2009. Map of the Salish Sea and Surrounding Basin.
French, S. & Romanowicz, B., 2014. Whole-mantle radially anisotropic shear-velocity structure from spectral-element waveform tomography, *Geophys. J. Int.,* **199,** 1303–1327.
Gowan, E.J., 2007, Glacio-isostatic adjustment modelling of improved relative sea-level observations in southwestern British Columbia, Canada, *MSc thesis*, 148pp., Univ. of Victoria, Victoria, B.C., Canada.
Hawley, W.B. & Allen, R.M., 2019. The fragmented death of the Farallon Plate, *Geophys. Res. Lett.,* **46** (13), 7386–7394.
Hawley, W.B., Allen, R.M. & Richards, M.A., 2016. Tomography reveals buoyant asthenosphere accumulating beneath the Juan de Fuca plate, *Science,* **353**(6306), 1406–1408.
Huang, P., Wu, P. & Steffen, H., 2019. In search of an ice history that is consistent with composite rheology in glacial isostatic adjustment modelling, *Earth planet. Sci. Lett.,* **517,** 26–37.
Hyndman, R.D. & Peacock, S.M., 2003. Serpentinization of the fore- arc mantle, *Earth Planet. Sci. Lett.,* **212,** 417–432.
James, T.S., Clague, J.J., Wang, K. & Hutchinson, I., 2000. Postglacial rebound at the northern Cascadia subduction zone, *Quater. Sci. Rev.,* **19,** 1527–1541.
James, T.S., Gowan, E.J., Hutchinson, I., Clague, J.J., Barrie, J.V. & Conway, K.W., 2009a. Sea-level change and paleogeographic reconstructions, southern Vancouver Island, British Columbia, Canada, *Quater. Sci. Rev.,* **28,** 1200–1216.
James, T.S., Gowan, E.J., Wada, I. & Wang, K., 2009b. Viscosity of the asthenosphere from glacial isostatic adjustment and subduction dynamics at the northern Cascadia subduction zone, British Columbia, Canada, *J. geophys. Res.,* **114,** doi:10.1029/2008JB006077.
James, T.S., Hutchinson, I., Barrie, J.V., Conway, K.W. & Mathews, D., 2005. Relative sea-level change in the northern Strait of Georgia, British Columbia, *Geogr. Phys. Quater.,* **59,** 113–127.
Karato, S., 2008. *Deformation of Earth Materials: An Introduction to the Rheology of the Solid Earth,* pp. 463, Cambridge Univ. Press.
Kendall, R., Mitrovica, J.X. & Milne, G.A., 2005. On post-glacial sea level - II. Numerical formulation and comparative results on spherically symmetric models, *Geophys. J. Int.,* **161**(3), 679–706.
Klemann, V., Ivins, E.R., Martinec, Z. & Wolf, D., 2007. Models of active glacial isostasy roofing warm subduction: case of the South Patagonian Ice Field, *J. geophys. Res.,* **112,** B09405, doi:10.1029/2006JB004818.
Kuchar, J., Milne, G.A. & Latychev, K., 2019. The importance of lateral Earth structure for North American glacial isostatic adjustment, *Earth planet. Sci. Lett.,* **512,** 236–245.
Lambeck, K., Rouby, H., Purcell, A., Sun, Y. & Sambridge, M., 2014. Sea level and global ice volumes from the last glacial maximum to the Holocene, *Proc. Natl. Acad. Sci.,* **111**(43), 15296–15303.
Lambeck, K., Smither, C. & Johnston, P., 1998. Sea-level change, glacial rebound and mantle viscosity for northern Europe, *Geophys. J. Int.,* **134,** 102–144.
Lamb, S., 2015. Kinematics to dynamics in the New Zealand Plate boundary zone: implications for the strength of the lithosphere, *Geophys. J. Int.,* **201**(2), 552–573.
Latychev, K., Mitrovica, J.X., Tamisiea, M.E., Tromp, J. & Moucha, R., 2005b. Influence of lithospheric thickness variations on 3-D crustal velocities due to glacial isostatic adjustment, *Geophys. Res. Lett.,* **32,** L01304, doi:10.1029/2004GL021454.

Latychev, K., Mitrovica, J.X., Tromp, J., Tamisiea, M., Komatitsch, D. & Christara, C., 2005a. Glacial isostatic adjustment on 3D earth models: a finite-volume formulation, *Geophys. J. Int.,* **161**(2), 421–444.

Li, T., Wu, P., Steffen, H. & Wang, H.S., 2018. In search of laterally heterogeneous viscosity models of glacial isostatic adjustment with the ICE-6G_C global ice history model, *Geophys. J. Int.,* **214,** 1191–1205.

Li, T. *et al.* 2020. Uncertainties of glacial isostatic adjustment model predictions in North America associated with 3D structure, *Geophys. Res. Let.,* **47,** 10.

Milne, G.A., Latychev, K., Schaeffer, A., Crowley, J.W., Lecavalier, B.S. & Audette, A., 2018. The influence of lateral Earth structure on glacial isostatic adjustment in Greenland, *Geophys. J. Int.,* **214,** 1252–1266.

Milne, G.A. & Mitrovica, J.X., 1998. Postglacial sea-level change on a rotating Earth, *Geophys. J. Int.,* **133,** 1–19.

Mitrovica, J.X., Forte, A.M. & Simons, M., 2000. A reappraisal of postglacial decay times from Richmond Gulf and James Bay, Canada, *Geophys. J. Int.,* **142**(3), 783–800.

Mitrovica, J.X. & Milne, G.A., 2003. On post-glacial sea level: I. General theory, *Geophys. J. Int.,* **154,** 253–267.

Mitrovica, J.X., Milne, G.A. & Davis, J.L., 2001. Glacial isostatic adjustment on a rotating Earth, *Geophys. J. Int.,* **147,** 562–579.

Mitrovica, J.X. & Peltier, W.R., 1989. Pleistocene deglaciation and the global gravity field, *J. geophys. Res.,* **94,** 13 651–13 671.

Mitrovica, J.X. & Peltier, W.R., 1993. A new formalism for inferring mantle viscosity based on estimates of post glacial decay times: application to RSL variations in N.E. Hudson Bay, *Geophys. Res. Lett.,* **20,** 2153–2186.

Mitrovica, J.X., Wahr, J., Matsuyama, I. & Paulson, A., 2005. The rotational stability of an ice-age earth, *Geophys. J. Int.,* **161**(2), 491–506.

Montillet, J.P., Melbourne, T.I. & Szeliga, W.M., 2018. GPS vertical land motion corrections to sea-level rise estimates in the Pacific Northwest, *J. geophys. Res*., **123**(2), 1196–1212.

Morell, K.D., Regalla, C., Leonard, L.J., Amos, C. & Levson, V., 2017. Quaternary rupture of a crustal fault beneath Victoria, British Columbia, Canada, *GSA Today,* **27**(3), 4–10.

Morell, K.D. *et al.* 2018. Holocene surface rupture history of an active forearc fault redefines seismic hazard in southwestern British Columbia, Canada, *Geophys. Res. Lett.,* **45,** 11 605–11 611.

Muhs, D.R., Simmons, K.R., Schumann, R.R., Groves, L.T., Mitrovica, J.X. & Laurel, D., 2012. Sea-level history during the last interglacial complex on San Nicolas Island, California: implications for glacial isostatic adjustment processes, paleozoogeography and tectonics, *Quater. Sci. Rev.,* **37,** 1–25.

Müller, R.D., Sdrolias, M., Gaina, C. & Roest, W.R., 2008. Age spreading rates and spreading asymmetry of the world's ocean crust, *Geochem., Geophys., Geosyst.,* **9,** Q04006, doi:10.1029/2007GC001743.

Nakada, M. & Lambeck, K., 1989. Late Pleistocene and Holocene sea-level change in the Australian region and made rheology, *Geophys. J. Int.,* **96,** 497–517.

Obrebski, M., Allen, R.M., Pollitz, F. & Hung, S.H., 2011. Lithosphere-asthenosphere interaction beneath the Western United States from the joint inversion of body-wave traveltimes and surface-wave phase velocities, *Geophys. J. Int.,* **185,** 1003–1021.

Paulson, A., Zhong, S. & Wahr, J., 2007. Inference of mantle viscosity from GRACE and relative sea level data, *Geophys. J. Int.,* **171,** 497–508.

Peltier, W.R., 2004. Global glacial isostasy and the surface of the ice-age Earth: the ICE-5G (VM2) model and GRACE, *Ann. Rev. Earth planet. Sci.,* **32,** 111–149.

Ranalli, G., 1998. Inferences on mantle rheology from creep laws, in *Dynamics of the Ice Age Earth—A Modern Perspective*, pp. 323–340, ed. Wu P., Trans Tech Publications.

Reynolds, L.C. & Simms, A.R., 2015. Late quaternary relative sea level in Southern California and Monterey Bay, *Quater. Sci. Rev.,* **126,** 57–66.

Ritsema, J., Deuss, A., van Heijst, H.J. & Woodhouse, J.H., 2011. S40RTS: a degree-40 shear-velocity model for the mantle from new Rayleigh wave dispersion, teleseismic traveltime and normal-mode splitting function measurements, *Geophys. J. Int.,* **184**(3), 1223–1236.

Roy, K. & Peltier, W.R., 2015. Glacial isostatic adjustment, relative sea level history and mantle viscosity: reconciling relative sea level model predictions for the U.S. east coast with geological constraints, *Geophy. J. Int.,* **201**(2), 1156–1181.

Schaeffer, A.J. & Lebedev, S., 2013. Global shear speed structure of the upper mantle and transition zone, *Geophys. J. Int.,* **194**(1), 417–449.

Severinghaus, J. & Atwater, T., 1990. Cenozoic geometry and thermal state of the subducting slabs beneath western North America, in *Basin and Range Extensional Tectonics Near the Latitude of Las Vegas,* Vol. **176,** ed. Wernicke, B.P., Geological Society of America Memoir.

Steffen, R., Audet, P. & Lund, B., 2018. Weakened lithosphere beneath Greenland inferred from effective elastic thickness: a hot spot effect? *Geophys. Res. Lett.,* **45,** 4733–4742.

Steffen, R., Steffen, H., Weiss, R., Lecavalier, B.S., Milne, G.A., Woodroffe, S.A. & Bennike, O., 2020. Early Holocene Greenland-ice mass loss likely triggered earthquakes and tsunami, *Earth planet. Sci. Lett.,* **546,** 116443.

Suito, H. & Freymueller, J.T., 2009. A viscoelastic and afterslip postseismic deformation model for the 1964 Alaska earthquake, *J. geophys. Res.,* **114,** B11404, doi:10.1029/2008JB005954.

Tarasov, L., Dyke, A.S., Neal, R.M. & Peltier, W.R., 2012. A data calibrated distribution of deglacial chronologies for the North American ice complex from glaciological modeling, *Earth planet. Sci. Lett.,* **315–316,** 30–40.

Törnqvist, T.E., Rosenheim, B.E., Hu, P. & Fernandez, A.B., 2015. Radiocarbon dating and calibration, in *Handbook of Sea-Level Research,* pp. 349–360, eds Shennan, I., Long, A.J. & Horton, B.P., John Wiley & Sons, Ltd.

Ullman, D.J., Carlson, A.E., Hostetler, S.W., Clark, P.U., Cuzzone, J., Milne, G.A., Winsor, K. & Caffee, M., 2016. Final Laurentide ice-sheet deglaciation and Holocene climate-sea level change, *Quater. Sci. Rev.,* **152,** 49–59.

van der Wal, W., Barnhoorn, A., Stocchi, P., Gradmann, S., Wu, P., Drury, M. & Vermeersen, L.L.A., 2013. Glacial isostatic adjustment model with composite 3D earth rheology for Fennoscandia, *Geophys. J. Int.,* **194**(1), 61–77.

van der Wal, W., Whitehouse, P.L. & Schrama, E.J.O., 2015. Effect of GIA models with 3D composite mantle viscosity on GRACE mass balance estimates for Antarctica, *Earth planet. Sci. Lett.,* **414,** doi:10.1016/j.epsl.2015.01.001.

Wada, I., Wang, K., He, J. & Hyndman, R.D., 2008. Weakening of the subduction interface and its effects on surface heat flow, slab dehydration, and mantle wedge serpentinization, *J. geophys. Res.,* **113,** B04402, doi 10.1029/2007JB005190.

Wang, H., Wu, P. & van der Wal, W., 2008. Using postglacial sea level, crustal velocities and gravity-rate-of-change to constrain the influence of thermal effects on mantle lateral heterogeneities, *J. Geodyn.,* **46,** 104–117.

Wang, K., Dragert, H. & Melosh, H.J., 1994. Finite element study of uplif and strain across Vancouver Island *Can. J. Earth Sci.,* **31,** 1510–1522.

Watts, A.B., 2001. *Isostasy and Flexure of the Lithosphere,* Cambridge Univ. Press, 458.

Wu, P. & Peltier, W.R., 1982. Viscous gravitational relaxation, *Geophys. J. R. astr. Soc.,* **70,** 435–486.

Wu, P. & Van Der Wal, W., 2003. Postglacial sea levels on a spherical, self-gravitating viscoelastic earth: effects of lateral viscosity variations in the upper mantle on the inference of viscosity contrasts in the lower mantle, *Earth planet. Sci. Lett.,* **211**(1), 57–68.

Wu, P. & Wang, H., 2008. Postglacial isostatic adjustment in a selfgravitating spherical earth with power-law rheology, *J. Geodyn.,* **46,** 118–130.

Wu, P., Wang, H. & Steffen, H., 2013. The role of thermal effect on mantle seismic anomalies under Laurentia and Fennoscandia from observations of glacial isostatic adjustment, *Geophys. J. Int.,* **192**(1), 7–17.

Xue, M. & Allen, R.M., 2010. Mantle structure beneath the western United States and its implications for convection processes, *J. geophys. Res.,* **115,** B07303, doi:10.1029/2008JB006079.

Yousefi, M., Milne, G.A., Love, R. & Tarasov, L., 2018. Glacial isostatic adjustment along the Pacific coast of central North America, *Quater. Sci. Rev.,* **193,** 288–311.

Zandt, G., Gilbert, H., Owens, T.J., Ducea, M., Saleeby, J. & Jones, C.H., 2004. Active foundering of a continental arc root beneath the southern Sierra Nevada in California, *Nature,* **431,** 41–46.

Zhong, S.J., Paulson, A. & Wahr, J., 2003. Three-dimensional finite element modelling of Earth's viscoelastic deformation: effects of lateral variations in lithospheric thickness, *Geophys. J. Int.,* **155,** 679–695.